

Hybrid Quantum and Classical Simulations of the Dihydrofolate Reductase Catalyzed Hydride Transfer Reaction on an Accurate Semi-Empirical Potential Energy Surface

Dvir Doron,[†] Dan Thomas Major,^{*,†} Amnon Kohen,[‡] Walter Thiel,[§] and Xin Wu[§]

[†]Department of Chemistry, The Lise Meitner-Minerva Center of Computational Quantum Chemistry, Bar-Ilan University, Ramat-Gan 52900, Israel

[‡]Department of Chemistry, University of Iowa, Iowa City, Iowa 52242, United States

[§]Max-Planck-Institut für Kohlenforschung, Kaiser-Wilhelm-Platz 1, D-45470 Mülheim an der Ruhr, Germany

S Supporting Information

ABSTRACT: Dihydrofolate reductase (DHFR) catalyzes the reduction of 7,8-dihydrofolate by nicotinamide adenine dinucleotide phosphate hydride (NADPH) to form 5,6,7,8-tetrahydrofolate and oxidized nicotinamide. DHFR is a small, flexible, monomeric protein with no metals or SS bonds and serves as one of the enzymes commonly used to examine basic aspects in enzymology. In the current work, we present extensive benchmark calculations for several model reactions in the gas phase that are relevant to the DHFR catalyzed hydride transfer. To this end, we employ G4MP2 and CBS-QB3 ab initio calculations as well as numerous density functional theory methods. Using these results, we develop two specific reaction parameter (SRP) Hamiltonians based on the semiempirical AM1 method. The first generation SRP Hamiltonian does not account for dispersion, while the second generation SRP accounts for dispersion implicitly via the AM1 core-repulsion functions. These SRP semiempirical Hamiltonians are subsequently used in hybrid quantum mechanics/molecular mechanics simulations of the DHFR catalyzed reaction. Finally, kinetic isotope effects are computed using a mass-perturbation-based path-integral approach.

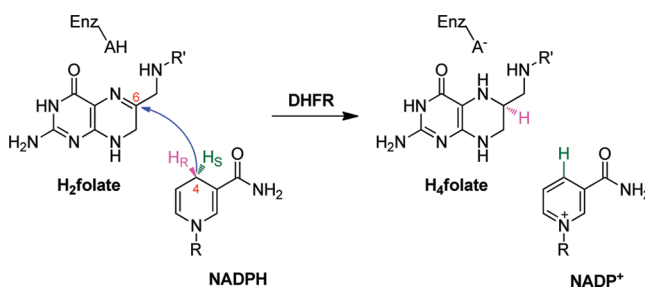
INTRODUCTION

Dihydrofolate reductase (DHFR; EC 1.5.1.3) catalyzes the reduction of 7,8-dihydrofolate (H_2 folate) by nicotinamide adenine dinucleotide phosphate hydride (NADPH) to form 5,6,7,8-tetrahydrofolate (H_4 folate) and $NADP^+$. Its principal function is to maintain intracellular pools of H_4 folate, which in turn serves as a cofactor in one-carbon metabolic processes and is essential for the biosynthesis of purines, thymine nucleotides, and several amino acids. DHFR has long been recognized as an important target for various therapeutic purposes, in particular the development of anticancer and antibacterial drugs, such as methotrexate and trimethoprim, respectively.^{1,2} The clinical importance of DHFR, along with its relatively modest size (159 aa in *E. coli* DHFR), has led many researchers to study, both experimentally and theoretically, the catalytic mechanism and kinetics of the NADPH-dependent hydride transfer reaction.¹

The key chemical step in the catalytic cycle of DHFR involves a stereospecific transfer of the *pro-R* hydrogen at the C4 position of the nicotinamide ring in NADPH to the *si*-face of the C6 atom of the pterin ring in H_2 folate, with concomitant protonation at the adjacent N5 position (Scheme 1).^{3,4}

Early kinetic studies of *E. coli* DHFR by Fierke et al. established a catalytic pathway cycling between five intermediates, including the $E \cdot NADPH$, the Michaelis complex $E \cdot NADPH \cdot H_2$ folate, the ternary product complex $E \cdot NADP^+ \cdot H_4$ folate, the binary product complex $E \cdot H_4$ folate, and the product release complex $E \cdot NADPH \cdot H_4$ folate.⁵ At neutral pH, the hydride-transfer rate in the wild-type enzyme is 220 s^{-1} and the rate-determining step is the release of the product H_4 folate (12 s^{-1}),

Scheme 1. Hydride Transfer Reaction Catalyzed by DHFR^a



^a R: adenine dinucleotide 2'-phosphate. R': *p*-aminobenzoyl-glutamate.

whereas at high pH, the hydride transfer step becomes more rate limiting, suggesting that the protonated substrate (henceforth H_3 folate⁺) is the reactive species for the hydride transfer reaction.⁵ Thus, the traditional view is that the protonation step precedes hydride transfer, thereby generating a resonance-stabilized iminium intermediate that serves as a more efficient acceptor toward the negatively charged hydride ion.^{4,6–8} Indeed, vibrational spectroscopic studies by Callender et al. have demonstrated that the N5 pK_a of H_2 folate is raised from 2.6 in solution to 6.5 in the ternary product complex with *E. coli* DHFR.^{9–12} The elevation of the N5 pK_a by four units upon complex formation is likely an enzymatic strategy for a substantial rate enhancement

Received: July 10, 2011

Published: August 26, 2011

over the uncatalyzed reaction in solution. It is likely that the hydrophobic nature of the active site pocket maintains a relatively low permittivity, thereby lowering $\text{H}_3\text{folate}^+$ acidity. Nevertheless, the protonation source is a rather controversial issue: originally, it was believed to be Asp27, being the only ionizable residue within the binding site of *E. coli* DHFR.^{10,13,14} However, the studies of Callender and co-workers suggested that the N5 atom is responsible for the pH dependency of the reaction and that the Asp27 residue exists in a deprotonated form at physiological pH and does not donate a proton to the substrate during enzymatic catalysis. It has been suggested instead that the negative charge of the carboxylate of Asp27 could stabilize the protonated substrate even though this group is on the other side of the bound substrate relative to N5.^{10,11,15} This notion was supported by computational studies of Brooks and Rod, arguing that the protonation of the substrate's N5 position comes directly from the bulk solvent.¹⁶

From a structural point of view, DHFR is a small monomeric protein (~ 18 kD, 159 aa for the *E. coli* DHFR).^{17–20} The substrate and coenzyme bind in a deep hydrophobic cleft at the juncture of the adenosine binding subdomain and the major (“loop”) subdomain. In its “closed” conformation, the Met20 loop (residues 9–24) lies directly over the active site, shielding the reactants from the solvent, and is primarily responsible for determining the active site architecture. X-ray studies in numerous ligand-bound states show that the Met20 loop assumes four characteristic conformations with respect to the active site.²⁰ In particular, the movement of Met20 loop and the cycling of the $\beta\text{F}-\beta\text{G}$ and $\beta\text{G}-\beta\text{H}$ loops between the *closed* and *occluded* conformations are coordinated with the stages of the catalytic cycle.²⁰

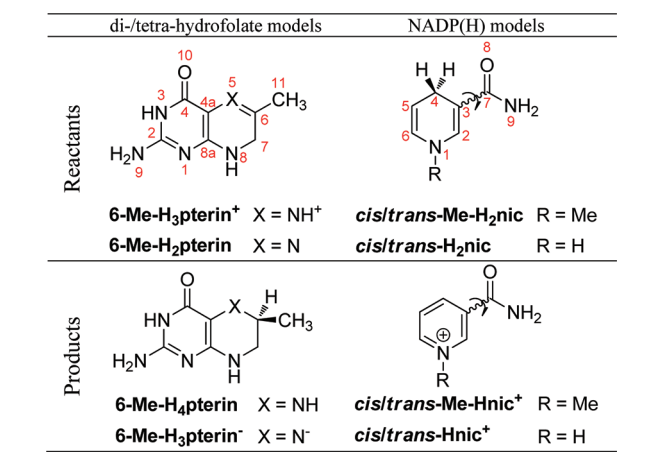
Early computational studies on the hydride transfer reaction catalyzed by DHFR were typically performed for small model systems *in vacuo*.^{21–24} In these studies, the potential energy surface (PES) was traditionally explored at the semiempirical or *ab initio* levels of theory. Subsequently, hybrid quantum-mechanical/molecular-mechanical (QM/MM) studies of DHFR have enabled the examination of environmental effects.^{4,25–27} Indeed, Moliner and co-workers in their pioneering QM/MM study on DHFR⁴ illustrated the importance of incorporating the enzyme's degrees of freedom in the study of transition state structures, compared to those calculated for the gas phase models.⁴ However, the calculated free energies of reaction and activation barriers by this approach were unrealistic compared to the experimental data, overestimating the free energy barrier for the enzymatic reaction, due to the inaccurate representation of the atoms in the QM region by a semiempirical method.

Nevertheless, numerous research groups took advantage of the computational efficiency of the hybrid semiempirical QM/MM approach combined with molecular dynamics (MD) simulations, to explore the hydride transfer reaction in DHFR^{7,28–30} and other related dehydrogenases.^{31–34} Some of these works^{7,28,30} attempted to compensate for the inherent errors in the semiempirical models by introducing correction terms. In particular, Gready and co-workers derived correction terms for selected configurations estimated from analogue cluster calculations at the DFT and post-Hartree–Fock theoretical levels, and these were applied to the activation free energy.²⁸ However, the authors did not manage to obtain quantitative agreement with the experimentally observed free energy barrier. On the other hand, Garcia-Viloca et al.,⁷ and more recently Brooks and Thorpe,³⁰ enhanced the semiempirical Hamiltonian with a simple valence bond (SVB) correction term,³⁵ which was parametrized to fit two quantities: the activation free energy of 13.4 kcal/mol,

which is predicted by transition-state theory expression taking the experimental pH-independent hydride transfer rate constant (950 s^{-1} at $25\text{ }^\circ\text{C}$)⁵ into account, and the reaction free energy of -4.4 kcal/mol, calculated from the reported equilibrium constant (1700).⁵ The disadvantage of such an approach is that for systems where the original QM method performs poorly, the SVB term is necessarily large. This may introduce artifacts into the vibrational frequency related to the SVB (reaction) coordinate, as well as an artificial increase in energy at the end points of the reaction coordinate.⁷ Such QM/MM potentials have been employed in combination with ensemble averaged variational transition state theory with multidimensional tunneling (EA-VTST/MT) calculations to obtain kinetic isotope effects.³⁶

A different QM/MM approach to studying hydride transfer reactions is the empirical valence bond (EVB) potential for the QM region, which was developed by Warshel and Weiss^{37,38} and parametrized for DHFR by Hammes-Schiffer et al.^{39,40} and Warshel and Liu.⁴¹ In this method, the hydride transfer reaction is represented by means of two empirical valence bond states, namely, reactants and products. The matrix elements between these diabatic states are represented as MM terms which are parametrized to reproduce experimental free energies of reaction and activation (dictated by either the pH-independent³⁹ or -dependent⁴⁰ intrinsic rate constants). An advantage of the EVB approach is that the reaction coordinate can naturally be expressed in terms of a collective entity (i.e., the energy gap between the reactant and product diabatic states). Additionally, the EVB method is computationally very efficient. On the other hand, due to its simplistic form and depending on the parametrization strategy, the fine details of the potential energy surface may not be described correctly. Furthermore, the experimental assessment of intrinsic rates in a complex kinetic cascade is limited, and the presumed experimental rate constant is commonly a complex kinetic term with many microscopic rate constants that cannot be distinguished experimentally. Therefore, using experimentally determined rate constants to parametrize the EVB terms might be problematic. The EVB potential has been employed to incorporate nuclear quantum effects by representing the transferring hydrogen nucleus as a 3-D vibrational wave function,³⁹ as well as in Feynman path-integral (PI) simulations.⁴² For a tabulated summary of some prominent computational studies on the DHFR hydride transfer reaction published in the past decade, the reader is referred to the Supporting Information.

To the best of our knowledge, no simulation of DHFR has gone beyond the EVB level or the semiempirical (AM1/PM3) Hamiltonian levels, using the standard parameters. In this paper, we first present gas-phase model calculations for the hydride transfer reaction between H_2folate and NADPH, using high-level *ab initio* and density functional theory methods. Although these models lack the contribution of the enzymatic environment, the calculations shed light on some key thermodynamic aspects related to the intrinsic thermochemistry of the reaction. Second, we present an accurate potential energy surface for the hydride transfer reaction in the enzyme *E. coli* DHFR, taking advantage of the comprehensive gas phase calculations presented herein. This potential energy surface is described by a hybrid quantum mechanics/molecular mechanics (QM/MM) potential, where the QM subsystem is treated by a semiempirical model that has been specifically parametrized to reproduce *ab initio* and DFT data. Consequently, the quality of such a specific reaction parameter (SRP) model^{43–45} is comparable with calculations at the *ab initio* and DFT levels, but at a considerably lower cost, hence

Chart 1. Main Models Subjected to Gas-Phase Calculations in This Study

allowing us to perform long MD simulations with the full solvated enzyme. The calibration of the AM1 Hamiltonian was performed only for the reaction in the gas phase (i.e., the intrinsic performance of the QM model), while the interactions with the environment are captured via the QM/MM interaction terms. Subsequently, the performance of the QM/MM potential was validated for the enzymatic reaction. This is in contrast to models employed in earlier studies, which parametrize empirical QM models such as EVB and SVB to the experimental free energies of reaction and activation in solution or in the enzyme. Two principle SRP models were explored, differing in the way they treat dispersion interactions. Nuclear quantum effects (NQE) are described using a coupled free-energy mass-perturbation and umbrella sampling simulation technique employing Feynman centroid path integral calculations (PI-FEP/UM).⁴⁶ Thus, both the electronic structure of the reacting system and the nuclear dynamics are treated quantum mechanically. This method has been demonstrated in a series of studies of chemical reactions in solution and in enzymes.^{44–48}

METHODOLOGY

Gas Phase QM Calculations. Model Reactions. The molecules depicted in Chart 1 represent chemical analogues of the reacting ligands and their corresponding products involved in the DHFR enzymatic reaction. The geometries were fully optimized in the gas phase using the Gaussian 09 program⁴⁹ and seven different density functionals, including one generalized gradient approximation (GGA) functional [PBE/PBE (PBE)⁵⁰], two hybrid GGA functionals [PBE1PBE (PBE0)⁵¹ and B3LYP^{52–54}], and four hybrid meta-GGA functionals (B98,⁵⁵ BB1K,⁵⁶ MPWB1K,⁵⁶ and M06⁵⁷). For any functional, the 6-31+G(d,p) basis set was found to give adequately converged geometries and reaction energies (results are not shown for other basis sets). The same geometries were recalculated with the semiempirical potential Austin Model 1 (AM1),⁵⁸ using the standard parameter scheme within Gaussian 09. We also carried out high-level calculations with the complete basis set method CBS-QB3,^{59,60} as well as the Gaussian theory method G4MP2.^{61,62} The latter method provided most of the target values for reparametrization of the AM1 Hamiltonian (*vide infra*).

The H₂folate substrate and its corresponding H₄folate product are represented by derivatives of 6-methyl-7,8-dihydropterin and

6-methyl-5,6,7,8-tetrahydropterin. These molecular models are the substrate and product of the DHFR catalyzed reaction, and it is assumed that the mechanism of reduction of the 7,8-dihydropterin is similar to that of 7,8-dihydrofolate.⁶³ To investigate the effect of protonation of the pyrazine's N5 atom on thermodynamics, two model reactions were inspected: the “protonated” model, which involves the protonated form of the dihydropterin reactant (6-Me-H₃pterin⁺), ending up in a neutral reduced tetrahydropterin product (6-Me-H₄pterin), and the “unprotonated” model, in which the unprotonated dihydropterin (6-Me-H₂pterin) is reduced to a negatively charged species (6-Me-H₃pterin⁻).

Two conformers of the nicotinamide derivative representing the NADP(H) cofactor were considered, distinguished by the orientation of the carboxamide with respect to the (dihydro)pyridine ring: the *cisoid* conformer, in which the carbonyl and the C2=C3 bond are quasi-synperiplanar, and the *transoid* conformer, where these two are quasi-antiperiplanar. As the two types of conformers were taken into account for both the reduced and oxidized nicotinamide species (Me-H₂nic and Me-Hnic⁺, respectively), four thermodynamic pathways were computed for each model reaction separately, as depicted in Scheme 2.

In both model reactions, the changes in electronic energy (ΔE_{el}), enthalpy (ΔH), and Gibbs free energy (ΔG) at 298 K were computed for each pathway with the aforementioned methods, according to the following general equations:

$$\Delta X_r^{\text{prot}} = X[6\text{-Me-H}_4\text{pterin}] + X[\text{cis/trans-Me-Hnic}^+] - X[6\text{-Me-H}_3\text{pterin}^+] - X[\text{cis/trans-Me-H}_2\text{nic}] \quad (1a)$$

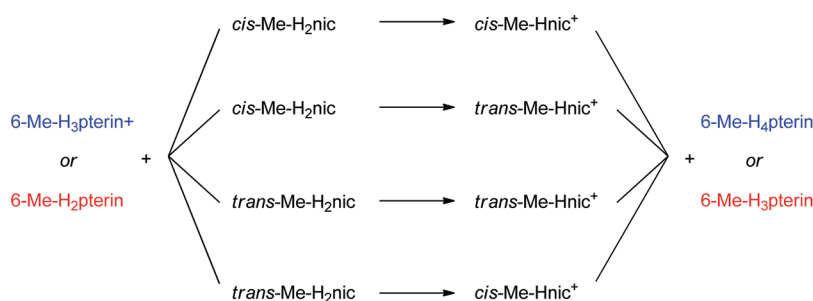
$$\Delta X_r^{\text{unprot}} = X[6\text{-Me-H}_3\text{pterin}^-] + X[\text{cis/trans-Me-Hnic}^+] - X[6\text{-Me-H}_2\text{pterin}] - X[\text{cis/trans-Me-H}_2\text{nic}] \quad (1b)$$

where X is a general notation for E_{el} , H , or G , and the superscripts X^{prot} and X^{unprot} refer to the protonated and unprotonated model reactions, respectively.

Modeling the Reactant, Transition, and Product State Complexes. The optimized model structure for the transition state complex was found using the synchronous transit-guided quasi-Newton (STQN) method⁶⁴ implemented in the Gaussian 09 program,⁴⁹ with all seven density functionals and the standard semiempirical AM1 potential (the G4MP2 method turned out to be too costly for transition state optimization of the bimolecular complex). In the case of the B3LYP functional, an empirical Grimme-type dispersion correction was also added (denoted B3LYP-D).^{65,66} The *transoid* conformer of the Me-H₂nic subunit was chosen, because it was found to be the most prevalent conformer identified in X-ray crystal structures of most enzyme active sites,^{67,68} in particular *E. coli* DHFR.²⁰ The saddle point was identified by a single imaginary vibrational frequency corresponding to the normal mode of transferring the hydride between the donor (C4 in the nicotinamide subunit) and acceptor (C6 in the pterin subunit) carbons.

The reactant and product complexes, [6-Me-H₃pterin⁺ · *trans*-Me-H₂nic] and [6-Me-H₄pterin · *trans*-Me-Hnic⁺], respectively, were obtained by intrinsic reaction coordinate (IRC) calculations in the direction of reactants and products. The steepest descent path in mass-scaled coordinates was followed using 100 steps of 0.1 Bohr in each direction of the reaction path

Scheme 2. Possible Thermodynamic Pathways for the Protonated (Blue) and Unprotonated (Red) Model Reactions of the Hydride Transfer in the Gas Phase



down to the reactant and product complex wells, where the root-mean-square gradient norms at the end points were no higher than $0.2 \text{ kcal} \cdot \text{mol}^{-1} \cdot \text{\AA}^{-1}$ and $0.3 \text{ kcal} \cdot \text{mol}^{-1} \cdot \text{\AA}^{-1}$ in the forward and reverse directions, respectively. Wherever methods accounting for dispersion (B3LYP-D and M06) were used, the IRC calculations were performed further until the default convergence criteria were reached in each IRC direction. The IRC end points were further geometry optimized as was done for the individual molecules.

Development of Semiempirical Specific Reaction Parameters. In the SRP approach,⁴³ the semiempirical parameters are optimized for a given system, i.e., here to treat the hydride transfer reaction in DHFR. More specifically, AM1-SRP parameters were developed to reproduce electronic and thermodynamic properties obtained from high-level QM calculations on representative molecular models in the gas phase (*vide supra*). For the majority of the modeled species, the reference method for the AM1 parametrization was the composite Gaussian method G4MP2,^{61,62} whereas target quantities associated with models of the reactant, transition, and product state bimolecular complexes were calculated using the B3LYP, B3LYP-D, and M06 hybrid functionals^{52–54} with the 6-31+G(d,p) basis set. The observables used as target values were enthalpies of formation, reaction energies, geometries, dipole moments, Mulliken charges, and vibrational frequencies.

Briefly, the current SRP strategy aims at two major goals: (1) an electronic PES which is of high accuracy, comparable to a high-level *ab initio* or DFT PES, and (2) absolute atomization energies which give rise to accurate heats of formation. The former goal allows the SRP model to be employed in MD simulations where all classical thermal effects are included directly via the propagation of Newton's equations of motion, while all quantum thermal effects are included via path-integral simulations or similar methods. The latter objective serves to limit deviations from the original AM1 parameter set (which has been optimized to reproduce heats of formation) to a minimum, as many basic molecular properties are treated well by AM1, although energy values are often not sufficiently accurate for quantitative comparison with experimental results. The SRP parameters are obtained by a nonlinear optimization, starting with the original AM1 parameters as the initial input.⁶⁹ The following general sequential optimization scheme is adopted: (1) First, optimize the one-center energies (U_{ss} and U_{pp}) and the resonance integrals (β_s and β_p), followed by the α parameters in the core-repulsion function (CRF). (2) Adjust the orbital exponents (ζ_s and ζ_p) together with the previously optimized parameters. (3) Adjust the one-center two-electron repulsion integrals G_{ss} , G_{sp} , G_{pp} , G_{p2} (or $G_{pp'}$),

and H_{sp} together with the previously optimized parameters. (4) Include the Gaussian CRF parameters L , M , and K together with the previously optimized parameters.

The training set for the optimizations consisted of the 12 individual molecules in Chart 1, plus the neutral nicotinamides, *trans*-nic and *cis*-nic. Additionally, the reactant, product, and transition states and selected structures along the IRC reaction paths were also included. All individual molecules were fully geometry optimized during the SRP parametrization, while the complexes were either partially or fully optimized. Single point calculations were carried out for the structures along the IRC.

In order to assess the importance of dispersion interactions, we attempted to implicitly include dispersion effects into the AM1-SRP model via the AM1 CRFs. In this approach, an improved SRP Hamiltonian was developed which implicitly accounts for dispersion. The motivation for including dispersion was provided by initial attempts to optimize the geometry of the reactant and product complexes using standard AM1. This led to unrealistic gas-phase structures, presumably due to the lack of dispersion interactions in standard AM1; for example, the two fragments in the product complex moved far apart (see Results and Discussion section). In order to capture the dispersion interactions implicitly, an empirical Grimme-type dispersion correction was added to the CRF in standard AM1, and thereafter all parameters in the Gaussian AM1 terms were reoptimized to best fit this dispersion-corrected CRF by using a nonlinear least-squares procedure (see Appendix A for technical details). The original CRF, the added dispersion corrections, the sum of these two terms, and the best fit Gaussian terms for the H–H, C–C, N–N, and O–O atom pairs are plotted in Figure 1. The sum and fitted curves for the first three pairs are visually almost indistinguishable, and there are merely minor variations of the standard AM1 CRF parameters (Figure 1). In the case of the O–O pair, the fitted Gaussian terms for oxygen, however, are not able to reproduce the attractive well in the van der Waals region due to the presence of two positive (repulsion) Gaussian functions ($K > 0$). Since oxygen is chemically less important for the DHFR reaction, the standard AM1 parameters for oxygen in the Gaussian terms were retained except in the very last step (4) of the SRP parametrization. The dispersion corrected CRF parameters for hydrogen, carbon, and nitrogen were used in the subsequent optimization procedure described above (fixed in steps 1–3, and adjusted in step 4).

Following the strategy outlined above, two SRP Hamiltonians were developed and employed in the simulations on DHFR. Specifically, an initial model termed AM1-SRP was designed, where the target complex structures and properties employed in the SRP development process were obtained from B3LYP.

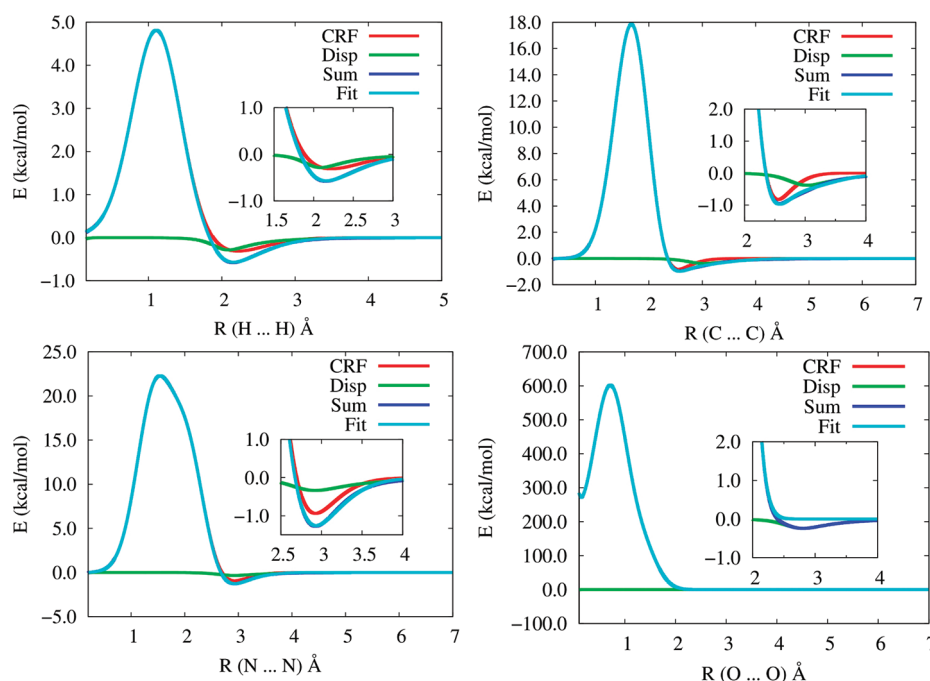


Figure 1. The nonlinear least-squares curve fittings for pairs of hydrogen, carbon, nitrogen, and oxygen atoms. CRF is the standard AM1 core repulsion function. Disp is the dispersion energy correction calculated using Grimme's formula. Sum is the total energy of CRF and Disp. Fit is the Gaussian term fitted with respect to Sum. A magnified subplot of the van der Waals region is also shown for each atom pair.

In this AM1-SRP model, intermolecular dispersion effects are not included during the parametrization process. Subsequently, a SRP Hamiltonian which implicitly includes dispersion was devised [termed AM1-SRP(D)]. Here, all complex structures were obtained from B3LYP-D calculations. In both approaches, the target data for the individual molecules were taken from G4MP2 calculations (accounting for intramolecular dispersion) at B3LYP optimized geometries.

Target values are presented in the Supporting Information, along with a detailed explanation of their determination, validation of the AM1-SRP performance, and a complete list of the modified parameters. The AM1-SRP results presented in the Supporting Information were obtained using the Gaussian 09 program.

Modeling QM/MM Interactions. To investigate the ability of the developed AM1-SRP Hamiltonians to accurately model QM/MM interactions, we computed the complexation energies between selected QM molecules and a TIP3P water molecule. The QM molecules are 6-Me-H₃pterin⁺, *trans*-Me-H₂nic, 6-Me-H₄pterin, and *trans*-Me-H₂nic⁺. For each of these QM moieties, a single TIP3P water molecule was placed at different hydrogen bonding positions around the molecule, for a total of up to four complexes per QM molecule. The QM/MM complexation energies were compared to complexation energies computed using various high-level methods.

QM/MM Simulations of *E. coli* DHFR. *Model of the Ternary Complex of E. coli DHFR.* The crystal structure of *E. coli* DHFR with folate and the oxidized cofactor NADP⁺ (PDB ID code: 1rx2), originally reported by Sawaya and Kraut,²⁰ was used to construct the initial configuration for the present study. This structure corresponds to the Michaelis complex of *E. coli* DHFR with the Met20 loop in the closed conformation. The X-ray crystal structure contains a total of 159 amino acid residues, 153 crystallographic waters, and the folate and NADP⁺ ligands,²⁰ which were replaced by H₂folate and NADPH, respectively, for

the simulation. The N5 atom on the substrate's pyrazine ring was protonated, as this form is thought to be the active species for the hydride transfer reaction.^{11,70}

On the basis of the results of Callender and co-workers,^{10,11,15} Asp27 was assumed to be deprotonated at neutral pH, while the protonation states for all other ionizable residues were set corresponding to pH 7.^{5,71,72} The hydrogen bonding patterns of the ionizable residues with the surrounding environment were visually inspected to verify that the protonation states are reasonable. The coordinates of hydrogen atoms of the protein, water, and coenzyme were determined using the HBUILD facility in the program CHARMM.^{73,74} The possible protonation states of histidine residues (proton on Ne, proton on Nd, or doubly protonated form) were determined by examination of the hydrogen bonding interactions. Peripheral/surface His residues were generally assumed to be positively charged. In NADPH, the 2'-phosphate moiety on the adenosine ribose was treated as a dianion, based on a pK_a of ~5.9 reported for NADP⁺ bound in cytochrome P-450 oxidoreductase (P-450R).⁷⁵ The coordinates of NE2 and OE1 atoms of the carboxamide moiety in the Gln102 residue were swapped, with respect to the original solved crystal structure, in order to form plausible hydrogen bond interactions with the adenine group of NADPH (a similar analysis was carried out by Brooks et al.⁷⁶). Residue 37 was built as Asp37 to be consistent with the 1RX2 PDB entry and previous work on DHFR, although sequencing data suggest that this residue might be Asn37.^{77,78} We note that the DHFR function is insensitive to the nature of the amino acid at position 37.⁷⁹ The resulting negatively charged enzyme (−14) has dimensions of ca. 34 × 42 × 50 Å³. To this system, we added 14 sodium ions in random positions outside the protein to obtain a net-neutral system, a prerequisite for convergence of the Ewald summation method (*vide infra*).⁸⁰ Subsequently, the protein, ligands, crystal waters, and counterions were embedded in a water box as detailed below.

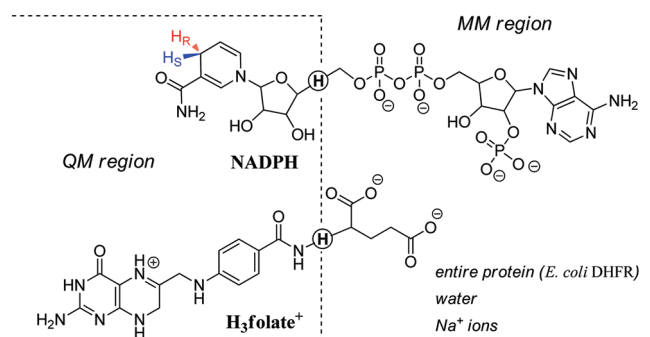


Figure 2. QM/MM partitioning scheme. The dashed line divides the QM and MM regions, and the quantum hydrogen link atoms are circled.

Hybrid QM(SRP)/MM Potential Energy Surface. The hydride transfer reaction in *E. coli* DHFR was described using a hybrid QM/MM potential energy surface.

$$\hat{H} = \hat{H}_{\text{QM}} + \hat{H}_{\text{MM}} + \hat{H}_{\text{QM/MM}} \quad (2)$$

The system was partitioned into a QM region consisting of 69 atoms and a MM region containing the rest of the system. The QM subsystem includes 38 atoms from the $\text{H}_3\text{folate}^+$ substrate (the pterin ring, the *N*-methylene-substituted *p*-aminobenzoyl (pABA) moiety, and the NH atoms of the glutamate moiety) and 29 atoms from the NADPH coenzyme (the dihydronicotinamide and ribose rings). In addition, two hydrogen link atoms were introduced along the covalent bonds crossing the boundary between the QM and the MM regions, to satisfy the valence requirements of the QM fragments. A schematic representation is depicted in Figure 2, where the quantum link atoms are circled.

The QM region was treated by the AM1-SRP or the AM1-SRP(D) Hamiltonians described above. The all-atom CHARMM22 force field⁸¹ with grid-based energy correction maps (CMAP)⁸² for peptide dihedral angles was employed to treat the entire protein, the substrate, and the ions, while the CHARMM27 force field⁸¹ was used for the coenzyme. The water molecules were represented by the three-point charge TIP3P model.⁸³ Atom types and parameters for the substrate were assigned by analogy with existing functional groups, as reported by Garcia-Viloca et al.⁷ For structure minimization and initial equilibration at the pure MM level, partial atomic charges for the substrate were assigned using the CHARMM force field (Momany-Rone) integrated in Discovery Studio 2.5 (Accelrys Software Inc., San Diego, CA).

QM/MM interactions were treated by electrostatic embedding wherein the MM partial atomic charges are included in the one-electron Hamiltonian. To fine-tune the PES, QM/MM interaction energies between the reacting fragments (QM) and the protein (MM) were modified. The van der Waals (vdW) parameters of the QM hydrogen atoms were changed to those that reproduce the interaction energies for hydrogen bonded complexes in the gas phase obtained from *ab initio* calculations at the MP2/6-31G(d,p) level.⁸⁴

Free-Energy Simulations—General Approach.⁴⁶ We follow a two-step procedure⁸⁵ in which we first carry out Newtonian MD simulations to determine the classical mechanical potential of mean force (PMF) along the reaction coordinate for the hydride transfer reaction between $\text{H}_3\text{folate}^+$ and NADPH in the fully solvated enzyme. Then, atoms that are directly involved in the hydride transfer are quantized, and the configurations sampled in

MD simulations are used in path-integral simulations by constraining the centroid positions of the quantized particles to the classical coordinates. This double (quantum and classical) averaging scheme is formally rigorous^{46,85–88} and yields the QM-PMF as a function of the centroid reaction path.^{89,90} In PI-FEP/UM, the ratio of the quantum partition functions for different isotopes, which yields the kinetic isotope effects (KIEs), is obtained by free-energy perturbation from a light isotope mass into a heavier one within the same centroid path-integral simulation,⁴⁶ avoiding the difference between two free-energy barriers with greater fluctuations than the difference itself for the two isotopic reactions. Consequently, the PI-FEP/UM method is unique in that it yields accurate results for computed KIEs, including secondary KIEs.^{45,46}

MD Simulations. MD simulations were conducted under periodic boundary conditions (PBC), with Ewald summation for electrostatic interactions.⁹¹ The solute was soaked in a pre-equilibrated $65 \times 65 \times 65 \text{ \AA}^3$ cubic box of 9461 water molecules, with its longest axis lying along the space diagonal of the box to ensure that all protein atoms are at least 10 \AA away from the edges of the box. The final model contained 27 986 atoms. For van der Waals and electrostatic interactions, a 13.0 \AA group-based cutoff was used. The Ewald method was employed for reciprocal space summations between MM sites as well as for the QM/MM interactions using a $64 \times 64 \times 64$ FFT grid.⁹¹ The κ value was set to 0.340 \AA^{-1} .

All water molecules were relaxed using the adopted-basis set Newton–Raphson (ABNR) minimization method (30 steps), while the crystal water oxygens were harmonically restrained to their original positions. This was followed by a 100 ps MD equilibration of the water molecules, which were thereafter minimized again (30 steps ABNR). Afterward, all atoms were subjected to minimization in a stepwise fashion, to remove close contacts in the initial protein–ligand–solvent system: (a) The substrate and coenzyme molecules were first minimized (30 step ABNR) while placing harmonic restraints on heavy atoms and keeping the rest of the system fixed. The restraints were gradually decreased to zero, while the ligands were further minimized (5×30 steps ABNR). (b) The water molecules and protein molecules were minimized (this time the ligands were held fixed) while the harmonic restraints on their heavy atoms were gradually diminished (4×10 steps ABNR). (c) Eventually, the whole system was minimized (30 steps ABNR) without any restraints.

The isothermal–isobaric ensemble (NPT) was employed at 1 atm and 298 K using the extended system pressure/temperature (CPT) algorithm of Andersen⁹² with an effective mass of 500 amu and a Hoover thermostat⁹³ with an effective mass of $1000 \text{ kcal/mol} \cdot \text{ps}^2$. The SHAKE algorithm⁹⁴ was applied to constrain all MM bonds involving hydrogen atoms, allowing a time-step of 1 fs. The system was gradually heated up from 48 to 298 K during five sessions of 5 ps for a total of 25 ps and thereafter equilibrated at the target temperature (298 K) over the course of 1 ns at the MM level of theory, with a further 200 ps of equilibration using the QM(SRP)/MM potential.

In light of the flexibility of the protein and the structural manipulation of the original ligands bound in the crystal structure, some issues emerged during the equilibration phase which required intervention. This included transient introduction of nuclear Overhauser effect (NOE) harmonic restraints on the distance between hydride donor and acceptor carbons (C4N in NADPH and C6 in $\text{H}_3\text{folate}^+$, respectively), as well as on other distances between donors and acceptors of selected hydrogen bonds within the protein which are characteristic of the closed

conformation (for details, see the Supporting Information). All restraints were removed 100 ps prior to commencing the production phase.

Potential of Mean Force. The classical-mechanical potential of mean force (CM-PMF)⁹⁵ was determined using the umbrella sampling technique, in order to sample the high-energy regions of the potential energy surface.⁹⁶ The reaction coordinate (ξ) was defined geometrically as the difference between the lengths of the breaking (C4N_{NADPH}–H4N) and forming (H4N–C6_{H₃folate}⁺) bonds. A total of 13 discrete regions along the reaction coordinate (“windows”) were defined with a uniform spacing of 0.25 Å. Each simulation was performed with the addition of a biasing potential (roughly the negative of the computed PMF), and a harmonic restraint centered at each window. The harmonic force constants, k , ranged between 20.0 and 60.0 kcal·mol^{−1}·Å^{−2} [$E_{\text{harm}} = k(\xi - \xi_{\text{ref}})^2$]. Each window was equilibrated for 2 ps, followed by a 100 ps production simulation that collected the probability densities of configurations (ρ) along the reaction coordinate (ξ) and sorted them into bins of width 0.01 Å. The coordinates were saved every 0.5 ps, and the velocities and positions of the last configuration generated in each window were used to initiate the next window. The PMF curve was obtained using the weighted histogram analysis method (WHAM).⁹⁷ To ensure convergence of the PMF, the simulations were run until the difference between sequential PMF profiles was less than ± 1 kcal/mol. The QM-PMF was obtained using a double averaging procedure by centroid path-integral simulations on configurations saved during the umbrella sampling.^{46,85,87} In essence, the centroid path-integral simulations yield the free energy difference between the classical mechanical and the quantum mechanical PMFs.^{46,85,87} For each isotope, a quantized correction curve was fit to the PI simulation data using an inverted Eckart function. The curve fitting was done using the Levenberg–Marquardt algorithm, and the inverted Eckart potential was added to the CM-PMF to obtain the QM-PMF.

Kinetic Isotope Effects. For the primary KIE ($k_{\text{H}}^{\text{H}}/k_{\text{D}}^{\text{H}}$), the *pro-R* hydrogen (the donated hydride, H4N) is substituted with deuterium, whereas the secondary KIE ($k_{\text{H}}^{\text{H}}/k_{\text{H}}^{\text{D}}$) involves the geminal *pro-S* hydrogen (H42N). To evaluate the KIEs, the centroid path-integral simulations were carried out for the light isotopic reaction, and the ratio of the partition functions between two isotopic reactions was determined by free-energy perturbation theory from the light mass into a heavier one.⁴⁶ In the present study, we quantized the donor (C4N_{NADPH}) and acceptor (C6_{H₃folate}⁺) carbons, in addition to the *pro-R* (H4N) and *pro-S* (H42N) hydrogens connected to the donor carbon (in the reactant state). Each quantized particle was represented by 32 beads. We used a bisection sampling technique⁸⁸ in all centroid path-integral simulations, and 10 free-particle configurations were sampled for each of 10 200 classical configurations, yielding a total of 102 000 path-integral sampling steps.

RESULTS AND DISCUSSION

Gas Phase QM Calculations. Optimized Geometries. According to the X-ray crystal structure of synthetically prepared 6-methyl-7,8-dihydropterin-monohydrochloride-monohydrate (6-Me-H₂pterin·HCl, which is essentially 6-Me-H₃pterin⁺), the heterocyclic ring members form a perfectly planar structure.⁹⁸ However, our gas phase DFT calculations, in particular at the B3LYP/6-31G(2df,p) level, suggest that the framework of the pyrazine ring in the dihydropterins is not completely planar, but

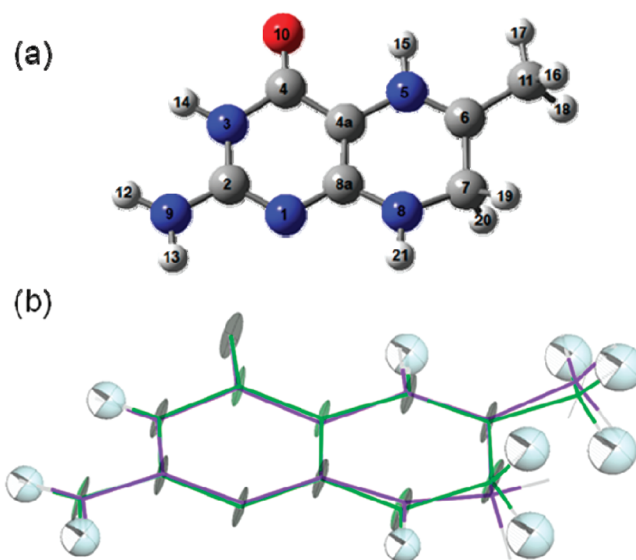


Figure 3. (a) Optimized geometry of 6-Me-H₃pterin⁺ calculated at the B3LYP/6-31G(2df,p) level of theory. (b) Superimposition of the X-ray crystal structure of 6-methyl-7,8-dihydropterin-monohydrochloride-monohydrate (green) with the computed geometry of 6-Me-H₃pterin⁺ (purple). Isotropic and anisotropic temperature factors corresponding to atoms in the crystal structure are represented by thermal ellipsoids.

rather a pucker is observed as the C7 methylene carbon projects above or below the plane formed by all other ring atoms (Figure 3). The magnitude of deviation from the plane varies with the selection of the method and basis set. MP2/6-311+G(2d,p) optimization supports the nonplanar nature of 6-Me-H₃pterin⁺ predicted by DFT. The discrepancy between experimental results and theory could be due to crystal forces in the experimental structure. Conversely, the observed crystal structure could be the average of two structures puckered in opposite directions. As for the reduced equilibrium structures (6-Me-H₄pterin and 6-Me-H₃pterin[−]), the pyrazine ring adopts a half-chair conformation, where C6 and C7 lie below and above the plane, respectively, in a staggered conformation with respect to each other, and the methyl group attached to C6 takes a pseudo-equatorial position. These findings are in good agreement with ¹H NMR studies on tetrahydropterin derivatives (spin–spin coupling constants measurements).^{99–102} A comparison of the crystal structure of 6-Me-H₃pterin⁺ and the computed geometry at the B3LYP/6-31G(2df,p) level is available in the Supporting Information.

The degree of pyramidalization of the C2-exocyclic amino group can be defined by its torsion angles and tilting from the plane. While in the 6-Me-H₃pterin⁺ structure, this group is nearly coplanar with the 4-oxypyrimidine ring, it exhibits a substantial pyramidalization in the other pterin derivatives examined. As this amino group can be seen as a fragment of a guanidine-like moiety, it is relevant to mention that the solid-state structure of free base guanidine, recently determined by X-ray diffraction,¹⁰³ indicates a nonplanar geometry with pyramidal amino groups, in accordance with earlier *ab initio* calculations.¹⁰⁴ A pyramidal geometry is also exhibited at the N8 position in 6-Me-H₃pterin[−] (but not in the oxidized form), as well as at the N5 site in 6-Me-H₄pterin.

As for the nicotinamides, it is noteworthy that the *cisoid* conformer was found to be slightly more stable *in vacuo* (with the exception of the unsubstituted neutral molecules, *cis/trans*-nic), while the conformer identified in X-ray crystal structures of many

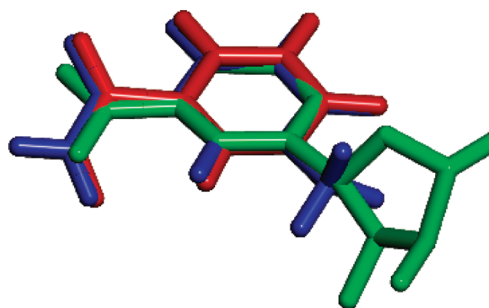


Figure 4. Superimposition of the oxidized nicotinamide portion in three models: segment from the NADP⁺ cofactor (green), coordinates taken from the crystal structure of *E. coli* DHFR ternary complex (PDB ID: 1rx2), *trans*-Me-Hnic⁺ (blue), and *trans*-Hnic⁺ (red) computed with B3LYP/6-31G(2df,p). Note the differences in the orientation of the carboxamide relative to the pyridine ring.

enzyme active sites is the *transoid* form.^{20,67,68} One may attribute the preference of the *transoid* species in the enzyme to specific interactions with the environment (hydrophilic/hydrophobic, polar/nonpolar), which may offset the relatively small energy difference between the two conformers.¹⁰⁵ There are some noticeable differences between the geometries of the *cisoid* and the *transoid* conformers. The degree of distortion of the carboxamide group with respect to the pyridine plane can be expressed in terms of the dihedral angle C2–C3–C7=O8 (Chart 1), as the difference between a “perfect” antiperiplanar angle (180°, for the *transoid* conformer) or synperiplanar angle (0°, for the *cisoid* conformer) and the actual dihedral. Calculations with B3LYP/6-31G(2df,p) suggest that in the *transoid* species, the carboxamide is rotated substantially out-of-plane, with distortions of 18.4–19.7° and 27.5–28.4° for the dihydronicotinamides and their corresponding oxidized counterparts. However, the out-of-plane rotations observed in the *cisoid* conformers are considerably smaller, with values of ca. 2.1° and 13.0–13.2° for H₂nic and Hnic⁺ derivatives, respectively. These observations are in agreement with previous theoretical studies.^{105–108} In the X-ray crystal structure of the ternary complex *ec*DHFR:folate:NADP⁺ (PDB code: 1rx2) used in the QM/MM simulations in this study, the nicotinamide subunit is found in its *transoid* conformer, with out-of-plane distortion of only 6° (Figure 4). Moreover, in most of the *transoid* conformers, there is a considerable pyramidalization of the amide nitrogen. These two geometric features of the carboxamide—the out-of-plane distortion and the *N*-pyramidalization—help to relieve unfavorable steric interactions between the NH₂ group and C2–H bond in the pyridine ring.

The 1,4-dihydropyridine ring skeleton in both unsubstituted and *N*-Me-substituted dihydronicotinamides is nearly planar, and no apparent puckering into a boat conformation is observed. This finding is in accord with X-ray data for some synthetically produced and isolated *N*-substituted nicotinamides, which are essentially planar in the dihydropyridine ring system.^{109,110}

Model Reactions. In Table 1, the calculated energies, enthalpies, and free energies at room temperature are given for the “protonated” (a) and “unprotonated” (b) model reactions involving *N*-methyl substituted nicotinamides. The results are reported separately for each of the four thermodynamic pathways described in the Methodology section (eqs 1a, 1b).

All methods except AM1 predict an exothermic (and exergonic) reaction for the “protonated” model. The reaction energies can be ordered in absolute magnitude as follows: *cisoid* → *transoid* <

cisoid → *cisoid* ≈ *transoid* → *transoid* < *transoid* → *cisoid* (this trend is opposite for the “unprotonated” model). The variation between these pathways stems from the slightly higher energy of the *transoid* conformer of the nicotinamide species relative to its *cisoid* counterpart, either in the reduced or oxidized form. For the density functionals, the relative order of Δ*E*_{el} (and generally also of Δ*H*_r and Δ*G*_r) in absolute values is PBEPBE < M06 < PBE1PBE < BB1K ≈ MPWB1K < B3LYP ≈ B98. The results obtained with CBS-QB3 and G4MP2 are almost identical yet considerably more exothermic than those obtained from DFT (Δ*E*_{el} being ~3 kcal/mol more negative than in the case of B3LYP, which is closest to the *ab initio* target data).

On the other hand, the “unprotonated” model reaction was found to be highly endothermic (and endergonic) with most of the computed Δ*G*_r values ranging between 120 and 134 kcal/mol. This emphasizes the crucial role of N5-protonation at the pyrazine ring of pterin in facilitating a thermodynamically feasible hydride transfer from dihydronicotinamide to dihydropterin in the gas phase.

Reaction, Transition, and Product Complexes. The diagram in Figure 5 compares the relative energies of the reactant, transition, and product states (RS, TS, and PS), for the reaction 6-Me-H₃pterin⁺ + *trans*-Me-H₂nic → 6-Me-H₄pterin + *trans*-Me-Hnic⁺, using AM1 and various density functionals.

Focusing on the bimolecular complexes, we define the energy barrier, Δ*E*[‡], as the energy gap between the TS and RS complexes, and the reaction energy Δ*E*_r as the difference between the PS and RS complexes. These quantities are poorly predicted by the standard AM1 method, as demonstrated by a high barrier (Δ*E*[‡] = 27.8 kcal/mol) and a slightly endothermic reaction (Δ*E*_r = 1.9 kcal/mol). The DFT methods suggest a much lower barrier and an exothermic reaction. The gradient corrected functional PBEPBE, which does not contain Hartree–Fock exchange, yields the lowest barrier, Δ*E*[‡] = 3.5 kcal/mol. There is good agreement between the functionals B3LYP, BB1K, MPWB1K, and M06, while B3LYP-D gives a slightly lower barrier. It is interesting to note that the computed gas-phase barriers (e.g., using M06, Δ*E*[‡] = 12.2 kcal/mol) are quite similar to the experimental free-energy barrier in the enzyme, 13.4 kcal/mol.⁵

The effect of dispersion is clearly seen by inspecting the energies of the fully separated molecules relative to the RS/PS complexes. Using the M06 and B3LYP-D functionals, which both account for dispersion interactions, there is a considerable additional stabilization of the complexes. At the B3LYP-D level, this dispersion effect may be estimated directly by comparing with B3LYP, yielding ca. 11 kcal/mol for the RS and PS. We note that the PS complexes presented in Figure 5 correspond to a nearly T-stacked conformation between the pterin and nicotinamide rings, similar to that found in DHFR. For methods that include dispersion, an additional minimum configuration corresponding to planar stacking between the rings is found. This point is discussed further below.

Considering the close agreement between B3LYP and M06 for the current system, we employ B3LYP (and B3LYP-D) as target data for the complexes in the SRP parametrization process. This choice is consistent with the target data for the individual molecules being taken from the G4MP2 approach, which employs B3LYP geometries and thermodynamic data.

SRP Development. The AM1 parameters were reoptimized against high-level QM results, obtained from G4MP2 calculations as well as B3LYP and B3LYP-D calculations with the 6-31+G(d,p) basis set. The properties used as target values

Table 1. Energetics Calculated for the “Protonated” (a) and “Unprotonated” (b) Model Reactions in the Gas Phase^a

method	Part a											
	<i>cisoid</i> → <i>cisoid</i> ^b			<i>cisoid</i> → <i>transoid</i> ^c			<i>transoid</i> → <i>transoid</i> ^d			<i>transoid</i> → <i>cisoid</i> ^e		
	ΔE_{el}	ΔH_{r}	ΔG_{r}	ΔE_{el}	ΔH_{r}	ΔG_{r}	ΔE_{el}	ΔH_{r}	ΔG_{r}	ΔE_{el}	ΔH_{r}	ΔG_{r}
AM1		7.4	8.5		9.0	9.8		7.1	7.6		5.5	6.4
B3LYP/6-31+G(d,p)	−7.5	−6.9	−6.6	−5.6	−5.0	−4.6	−7.7	−7.0	−7.0	−9.6	−9.0	−9.0
PBE1PBE/6-31+G(d,p)	−6.7	−6.1	−5.6	−4.7	−4.0	−3.8	−6.9	−6.3	−6.5	−8.8	−8.3	−8.3
PBEPBE/6-31+G(d,p)	−5.3	−4.6	−4.2	−3.5	−2.7	−2.8	−5.2	−4.7	−4.8	−7.0	−6.6	−6.2
B98/6-31+G(d,p)	−7.6	−7.0	−6.5	−5.7	−5.1	−5.5	−7.7	−7.2	−7.8	−9.6	−9.1	−8.7
BB1K/6-31+G(d,p)	−7.0	−6.5	−5.7	−4.9	−4.5	−4.5	−7.3	−6.8	−7.2	−9.4	−8.9	−8.5
MPWB1K/6-31+G(d,p)	−7.1	−6.7	−5.5	−5.0	−4.5	−5.1	−7.4	−6.9	−7.8	−9.5	−9.1	−8.2
M06/6-31+G(d,p)	−6.3	−5.8	−4.8	−4.5	−4.0	−2.2	−6.6	−6.0	−4.8	−8.4	−7.9	−7.4
G4MP2	−10.7	−10.1	−9.5	−8.7	−8.1	−7.6	−10.0	−9.5	−9.0	−12.0	−11.5	−10.9
CBS-QB3	−10.8	−10.1	−9.8	−8.7	−8.0	−7.7	−10.2	−9.6	−9.5	−12.2	−11.7	−11.6

method	Part b											
	<i>cisoid</i> → <i>cisoid</i> ^f			<i>cisoid</i> → <i>transoid</i> ^g			<i>transoid</i> → <i>transoid</i> ^h			<i>transoid</i> → <i>cisoid</i> ⁱ		
	ΔE_{el}	ΔH_{r}	ΔG_{r}	ΔE_{el}	ΔH_{r}	ΔG_{r}	ΔE_{el}	ΔH_{r}	ΔG_{r}	ΔE_{el}	ΔH_{r}	ΔG_{r}
AM1		129.6	130.7		131.1	132.0		129.2	129.8		127.7	128.6
B3LYP/6-31+G(d,p)	125.1	124.9	125.1	127.0	126.8	127.1	124.9	124.8	124.7	123.0	122.8	122.7
PBE1PBE/6-31+G(d,p)	127.2	126.8	127.2	129.2	128.8	129.0	127.0	126.5	126.3	125.1	124.5	124.5
PBEPBE/6-31+G(d,p)	121.7	121.1	121.2	123.5	122.9	122.6	121.8	120.9	120.5	120.0	119.1	119.1
B98/6-31+G(d,p)	125.5	124.9	125.4	127.4	126.9	126.3	125.4	124.8	124.0	123.6	122.9	123.1
BB1K/6-31+G(d,p)	131.4	131.0	131.8	133.6	133.0	133.0	131.2	130.7	130.3	129.1	128.6	129.1
MPWB1K/6-31+G(d,p)	131.7	131.2	132.5	133.9	133.3	132.9	131.5	131.0	130.2	129.3	128.8	129.8
M06/6-31+G(d,p)	129.0	128.2	129.0	130.8	130.1	131.6	128.7	128.0	129.0	126.9	126.2	126.4
G4MP2	124.9	124.3	124.7	126.9	126.3	126.5	125.6	125.0	125.1	123.6	123.0	123.2
CBS-QB3	125.2	124.6	124.7	127.2	126.7	126.8	125.8	125.1	125.0	123.7	123.0	122.9

^a ΔE_{el} is the change in electronic energy; ΔH_{r} and ΔG_{r} are the respective enthalpy and free energy changes at 298.15 K and 1 atm (including zero-point contributions). ^b 6-Me-H₃pterin⁺ + *cis*-Me-H₂nic ⇌ 6-Me-H₄pterin + *cis*-Me-Hnic⁺. ^c 6-Me-H₃pterin⁺ + *cis*-Me-H₂nic ⇌ 6-Me-H₄pterin + *trans*-Me-Hnic⁺. ^d 6-Me-H₃pterin⁺ + *trans*-Me-H₂nic ⇌ 6-Me-H₄pterin + *trans*-Me-Hnic⁺. ^e 6-Me-H₃pterin⁺ + *trans*-Me-H₂nic ⇌ 6-Me-H₄pterin + *cis*-Me-Hnic⁺. ^f 6-Me-H₂pterin + *cis*-Me-H₂nic ⇌ 6-Me-H₃pterin[−] + *cis*-Me-Hnic[−]. ^g 6-Me-H₂pterin + *cis*-Me-H₂nic ⇌ 6-Me-H₃pterin[−] + *trans*-Me-Hnic[−]. ^h 6-Me-H₂pterin + *trans*-Me-H₂nic ⇌ 6-Me-H₃pterin[−] + *trans*-Me-Hnic[−]. ⁱ 6-Me-H₂pterin + *trans*-Me-H₂nic ⇌ 6-Me-H₃pterin[−] + *cis*-Me-Hnic[−].

included heats of formation, dipole moments, Mulliken charges, and vibrational frequencies of the individual species. Furthermore, the reaction energies for the model complexes also served as reference data that contributed to the fitness function of the SRP model (*vide infra*), in order to improve the accuracy of the resulting PES.

Determination of the target heats of formation required some caution, as we are interested in a purely electronic structure description of the potential energy surface, while nuclear classical and quantum effects are added only at a later stage during enzyme simulations. Therefore, any thermal contribution should be excluded. On the other hand, the AM1 energies are originally interpreted in terms of heats of formations.⁵⁸ In the present AM1-SRP reparametrization, we mainly use *ab initio* and DFT energies as target data, and therefore the resulting AM1-SRP energies will mimic electronic energies. This allows the AM1-SRP models to be employed in molecular dynamics simulations where all classical thermal effects are included directly via the propagation of Newton's equations of motion, while all quantum thermal effects are included via path-integral simulations.

Table 2 compares the root-mean-square deviations (RMSD) from the target data for various properties calculated at the

optimized geometries in three parametrization schemes: standard AM1, AM1-SRP, and AM1-SRP(D). The target data for the 14 molecules are the same for the three parametrization schemes. The AM1-SRP parametrization did not involve the heats of formation of the pterin molecules due to the large gap between the corresponding target and AM1 values, an obstacle which was circumvented by minimizing the errors associated with related relative energies (see Table 3). Indeed, AM1-SRP produced the smallest RMSD errors in relative energies among the parametrization schemes, and the quality of the individual heats of formations was considerably improved by ca. 8 kcal/mol when going from standard AM1 to AM1-SRP. There were significant changes in the AM1-SRP(D) parameters compared with standard AM1, in particular in the Gaussian terms. This further reduced the RMSD error in the heats of formation to ca. 1 kcal/mol, including the pterin species (whose heats of formation were incorporated in the training set of AM1-SRP(D)). At the same time, the error in the relative energies was increased only slightly relative to AM1-SRP, making its energetic accuracy comparable to the latter. The RMSD error for the vibrational wavenumbers was reduced by 29 cm^{−1} and 55 cm^{−1} in AM1-SRP and AM1-SRP(D), respectively, relative to AM1. On the other hand, the

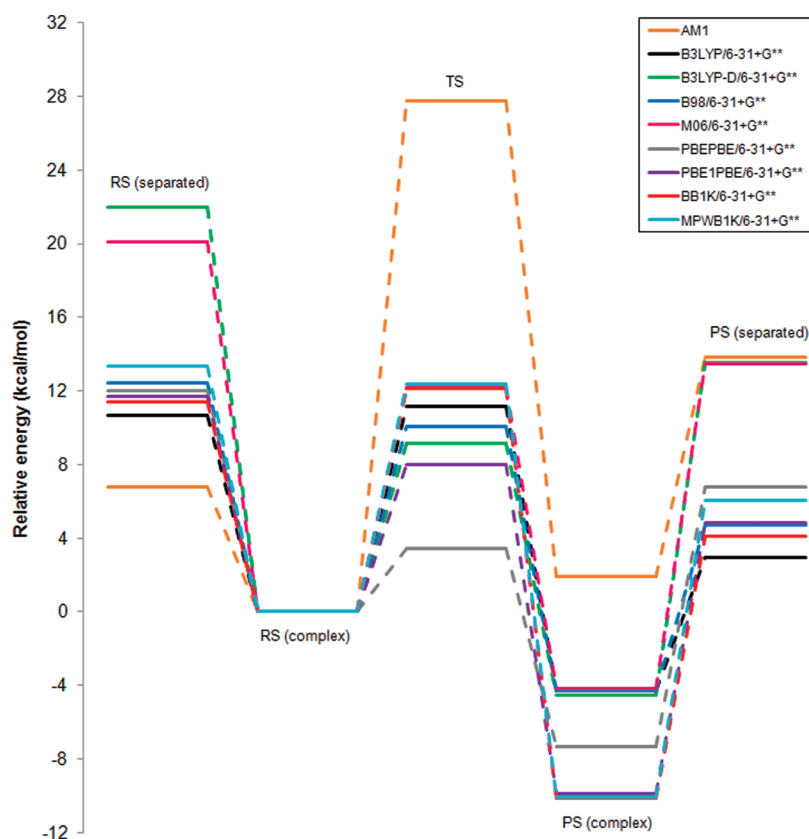


Figure 5. The relative energies (kcal/mol) of the reactant, transition, and product states associated with the reaction $6\text{-Me-H}_3\text{pterin}^+ + \text{trans-Me-H}_2\text{nic} \rightarrow 6\text{-Me-H}_4\text{pterin} + \text{trans-Me-Hnic}^+$. The fully separated reactants and products are represented by RS (separated) and PS (separated), respectively, where RS (complex) and PS (complex) refer to the corresponding bimolecular complexes.

Table 2. RMSD Errors for Properties Calculated at Optimized Geometries Using AM1, AM1-SRP, and AM1-SRP(D), with Respect to Target Values (G4MP2)

properties	AM1	AM1-SRP	AM1-SRP(D)
heats of formation ^a (kcal/mol)	12.1	3.8	1.3
relative energies ^b (kcal/mol)	9.5	1.9	2.2
bond lengths ^c (Å)	0.02	0.03	0.04
bond angles ^c (deg)	1.8	3.4	1.9
vibrational wavenumbers ^d (cm ⁻¹)	108	78	52
Mulliken atomic charges ^e (e)	0.16	0.27	0.20
dipole moments ^e (D)	1.27	1.08	(1.47)

^a The statistics refer to nicotinamide derivatives only. The target heats of formation for the pterin species were far off the AM1 values and were thus omitted from the calibration set for AM1-SRP [but included in the AM1-SRP(D) parametrization]. ^b The statistics refer to the reactions described in Table 3. ^c The statistics refer to all 14 individual species. ^d The statistics refer to wavenumbers larger than 2500 cm⁻¹ for all 14 individual species. ^e The statistics refer to eight neutral species out of the 14 individual species. Dipole moments were not included as reference data in the parametrization of AM1-SRP(D), hence the parentheses.

RMSD of the bond lengths, bond angles, and atomic charges calculated with AM1-SRP were slightly increased relative to AM1 by 0.01 Å, 1.6°, and 0.11e, whereas AM1-SRP(D) did somewhat better with 0.02 Å, 0.1°, and 0.04e, respectively. However, their overall quality was considered to be acceptable in light of the

large improvements for the energies and vibrational frequencies. The dipole moments calculated with all three schemes were of similar quality.

Table 3 provides further insight into the quality of selected relative energies obtained with each Hamiltonian. It lists the deviations for various reactions involving four and two species (classes I and II, respectively), with respect to the reference entries. As demonstrated by the total RMSD error for each class, AM1-SRP performs better for reactions of class I, while generally AM1-SRP(D) treats class II transitions more accurately (though to a less pronounced degree).

Having the tailored semiempirical Hamiltonians in hand, some structural and thermodynamic features of the reactant, transition, and product state complexes were analyzed and compared against the target DFT methods (Table 4). The analysis includes geometric relations between the hydride-donating and accepting carbons (C4' and C6, respectively) and the transferring hydride itself, as well as the imaginary vibrational frequency and energetic relations. The three complexes are depicted in Figure 6, comparing geometries that were obtained using DFT and SRP Hamiltonians.

Overall, there is good qualitative agreement between the computed semiempirical structures of the reactant and transition state complexes and the corresponding DFT reference structures, and the improvements of the SRP Hamiltonians over standard AM1 are substantial. In particular, the AM1-SRP Hamiltonian is able to reproduce the imaginary vibrational frequency of the reactive normal mode in the transition state as

Table 3. Signed Errors of Relative Energies (kcal/mol) Calculated with the AM1-SRP and AM1-SRP(D) Parameters, with Respect to the Target Data (G4MP2)^a

class	reaction	signed error (kcal/mol)		
		AM1	AM1-SRP	AM1-SRP(D)
I	6-Me-H ₃ pterin ⁺ + <i>trans</i> -Me-H ₂ nic → 6-Me-H ₄ pterin + <i>trans</i> -Me-Hnic ⁺	17.1	1.0	3.1
	6-Me-H ₃ pterin ⁺ + <i>cis</i> -Me-H ₂ nic → 6-Me-H ₄ pterin + <i>cis</i> -Me-Hnic ⁺	18.2	1.9	4.2
	6-Me-H ₃ pterin ⁺ + <i>trans</i> -H ₂ nic → 6-Me-H ₄ pterin + <i>trans</i> -Hnic ⁺	14.2	−2.3	−1.1
	6-Me-H ₃ pterin ⁺ + <i>cis</i> -H ₂ nic → 6-Me-H ₄ pterin + <i>cis</i> -Hnic ⁺	15.1	−1.4	−0.2
	6-Me-H ₂ pterin + <i>trans</i> -Me-H ₂ nic → 6-Me-H ₃ pterin [−] + <i>trans</i> -Me-Hnic ⁺	3.8	0.6	2.0
	6-Me-H ₂ pterin + <i>cis</i> -Me-H ₂ nic → 6-Me-H ₃ pterin [−] + <i>cis</i> -Me-Hnic ⁺	4.8	1.6	3.1
	6-Me-H ₂ pterin + <i>trans</i> -H ₂ nic → 6-Me-H ₃ pterin [−] + <i>trans</i> -Hnic ⁺	0.9	−2.7	−2.2
	6-Me-H ₂ pterin + <i>cis</i> -H ₂ nic → 6-Me-H ₃ pterin [−] + <i>cis</i> -Hnic ⁺	1.8	−1.7	−1.3
RMSD		11.7	1.8	2.5
II	6-Me-H ₃ pterin ⁺ $\xrightarrow{\text{H}^-}$ 6-Me-H ₄ pterin	15.7	1.6	1.3
	6-Me-H ₂ pterin $\xrightarrow{\text{H}^-}$ 6-Me-H ₃ pterin [−]	2.4	1.3	0.2
	<i>trans</i> -Me-H ₂ nic $\xrightarrow{\text{H}^-}$ <i>trans</i> -Me-Hnic ⁺	1.4	−0.6	1.8
	<i>cis</i> -Me-H ₂ nic $\xrightarrow{\text{H}^-}$ <i>cis</i> -Me-Hnic ⁺	2.5	0.3	3.0
	<i>trans</i> -H ₂ nic $\xrightarrow{\text{H}^-}$ <i>trans</i> -Hnic ⁺	−1.5	−3.9	−2.4
	<i>cis</i> -H ₂ nic $\xrightarrow{\text{H}^-}$ <i>cis</i> -Hnic ⁺	−0.6	−3.0	−1.5
	<i>cis</i> -nic → <i>trans</i> -nic	0.5	0.3	0.6
RMSD		6.1	2.1	1.8

^a Classes I and II assemble relative energies involving four and two species, respectively.

predicted by B3LYP/6-31+G(d,p) calculations (i.e., -880 cm^{-1} vs -838 cm^{-1}). On the other hand, the calculated imaginary frequency of the TS complex with AM1-SRP(D), -960 cm^{-1} , resembles more that predicted by M06, -953 cm^{-1} , than the corresponding B3LYP-D value, -716 cm^{-1} .

The energetic profiles obtained at different theoretical levels are presented in Figure 7. As expected, the AM1-SRP complexation energies are fairly close to those of B3LYP (-9.3 and -10.7 kcal/mol for RS, -3.0 and -7.2 kcal/mol for PS, respectively), while the AM1-SRP(D) results are similar to those of B3LYP-D (-22.8 and -22.0 kcal/mol for RS, -25.2 and -27.0 kcal/mol for PS; the counterpoise corrections for basis set superposition error (BSSE) with B3LYP-D are 1.5 and 2.1 kcal/mol for RS and PS, respectively). The barrier height obtained with AM1-SRP is 10.7 kcal/mol, comparable to 11.2 kcal/mol with B3LYP, while that obtained with AM1-SRP(D) is 13.6 kcal/mol, which is somewhat higher than the target value 9.2 kcal/mol obtained with B3LYP-D. In comparison, the M06 barrier height is 12.2 kcal/mol. An in-depth analysis of the RS and PS complexes will be presented below.

A detailed inspection of the geometry optimizations of the RS and PS complexes reveals that the PES in these regions is very flat with several plausible minima, particularly in the PS region. Using B3LYP and the AM1-SRP Hamiltonian, we could attain reasonable geometries of the RS and PS complexes via the IRC path from the TS only down to a certain point away from the TS in either direction (these structures are presented in Figure 6).

Full geometry optimization of the RS and PS complexes in the gas phase yielded highly distorted minimum structures, with no stacking, which do not resemble the configuration in the DHFR active site. As the two molecular segments in these complexes are weakly bound in the van der Waals region ($>3.5\text{ Å}$), it is necessary to include dispersion interactions (which are missing in the AM1 formalism) to accurately reproduce these geometries. Furthermore, the target complexes for AM1-SRP were derived from B3LYP calculations which do not include much dispersion. Indeed, the introduction of dispersion by means of B3LYP-D enabled us to obtain plausible minimum RS and PS geometries.

B3LYP-D and M06 optimizations of the PS both reveal two possible minimum configurations, with regard to the orientation of the nicotinamide ring toward the pterin fragment. (a) First is a “T-stacked” configuration, where the nicotinamide ring lies in a quasi-perpendicular plane with respect to the pterin ring. With this orientation, the complexation energy obtained with B3LYP-D is -18.1 kcal/mol , while M06 affords a related minimum geometry with a complexation energy of -17.6 kcal/mol . (b) Next is a fully “stacked” configuration, in which the rings are stacked one on top of the other, which corresponds to the global minimum of the PES of the PS complex (Figures 6 and 7). The B3LYP-D structure (complexation energy: -27.0 kcal/mol) is almost identical to the fully stacked complex obtained with M06 (-23.3 kcal/mol) and resembles that obtained with AM1-SRP(D) (-25.2 kcal/mol). With AM1-SRP(D), we could not find a partially T-stacked configuration, suggesting that this

Table 4. Geometric and Thermodynamic Properties of the Reactant, Transition and Product State Complexes in the Gas Phase, Calculated with Different Hamiltonians^a

complex	method	R (Å)			\angle C4'–H–C6 (deg)	IFreq (cm ^{−1})	ΔE (kcal/mol)
		C4'–H	C6–H	C4'–C6			
reactant state	AM1 ^b	1.128	2.640	3.636	146.61		0.0
	B3LYP/6-31+G(d,p) ^b	1.110	2.996	3.863	135.95		0.0
	AM1-SRP ^b	1.110	2.551	3.593	155.91		0.0
	B3LYP-D/6-31+G(d,p) ^c	1.103	2.751	3.500	124.85		0.0
	AM1-SRP(D) ^c	1.087	2.283	3.170	137.49		0.0
	M06 ^c	1.104	3.301	3.944	118.15		0.0
transition state	AM1	1.411	1.363	2.763	169.81	−1385	27.8
	B3LYP/6-31+G(d,p)	1.309	1.409	2.715	174.61	−838	11.2
	AM1-SRP	1.317	1.348	2.633	162.43	−880	10.7
	B3LYP-D/6-31+G(d,p)	1.280	1.396	2.664	169.09	−716	9.2
	AM1-SRP(D)	1.308	1.322	2.602	163.18	−960	13.6
	M06	1.313	1.362	2.667	171.01	−953	12.2
product state	AM1 ^b	2.512	1.136	3.507	145.37		1.9
	B3LYP/6-31+G(d,p) ^b	2.533	1.110	3.613	163.96		−4.3
	AM1-SRP ^b	2.514	1.116	3.503	147.07		−2.8
	B3LYP-D/6-31+G(d,p) ^{c,d}	2.679	1.110	3.632	143.52		−4.6
		(5.069)	(1.100)	(5.394)	(101.32)		(−13.5)
	AM1-SRP(D) ^c	4.248	1.092	4.748	110.82		−9.3
	M06 ^{c,d}	2.499	1.107	3.443	142.35		−4.2
		(5.034)	(1.107)	(5.706)	(107.44)		(−9.8)

^a C4' is the donor carbon in the nicotinamide subunit, C6 is the acceptor carbon in the pterin subunit, and H denotes the transferring hydride. IFreq is the imaginary frequency, and ΔE is the relative energy with respect to the reactant complex. ^b The final structure was obtained using IRC calculations. ^c The final structure was obtained using geometry optimization. ^d Values without parentheses refer to the local minimum structure with a “T-stacked” configuration. Values in parentheses refer to the fully stacked configuration, which corresponds to the global minimum on the potential energy surface.

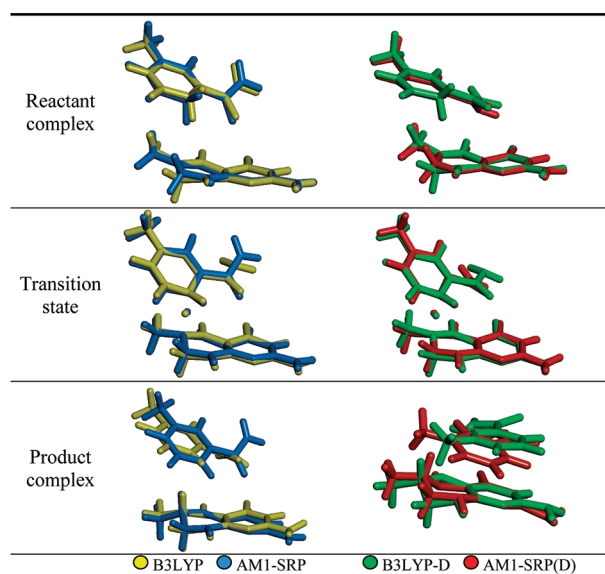


Figure 6. Structures of the reactant, transition, and product state complexes in the gas phase. The superimposed geometries were obtained by calculations at a DFT and a related semiempirical level. Structures are shown for two pairs of methods: B3LYP/6-31+G(d,p) and AM1-SRP and B3LYP-D/6-31+G(d,p) and AM1-SRP(D). The product state complexes represent the T-stacked configuration for B3LYP and AM1-SRP optimized structures and the fully stacked configuration for the B3LYP-D and AM1-SRP(D) optimized structures.

method might “over-stack” the PS complex. The greater stability of the fully stacked complexes may be attributed to the presence of dispersion interactions, hydrogen bonding interactions within the bimolecular complex, and close contacts between the π systems in the nicotinamide and pterin rings.

The gradient norm of the product complex during AM1-SRP(D) geometry optimization is plotted in Figure S1 (Supporting Information). The gradient is greatly reduced in the first steps. The PES then becomes quite flat and shallow. Thus, the structure of the product complex seems to be highly flexible, and many arrangements of the two molecular segments have relatively small gradients. The use of less stringent convergence criteria in the AM1-SRP(D) geometry optimization would have led to termination after about 100 cycles, at a structure close to the T-stacked configuration obtained with B3LYP-D (Figure S1).

QM/MM Interactions. To investigate the ability of the AM1-SRP Hamiltonians to accurately model QM/MM interactions, we computed the complexation energies between selected QM moieties (6-Me-H₃pterin⁺, *trans*-Me-H₂nic, 6-Me-H₄pterin, and *trans*-Me-Hnic⁺) and a TIP3P water molecule. For each of these QM moieties, a single water molecule was placed at different hydrogen bonding positions around the molecule, for a total of 14 QM/MM complexes (Table S8a, Supporting Information). The QM/MM interaction energies were computed using AM1, AM1-SRP, or AM1-SRP(D) and a TIP3P water molecule. These interaction energies were compared with data from M06, B3LYP-D, B3LYP, and HF, all in conjunction with the

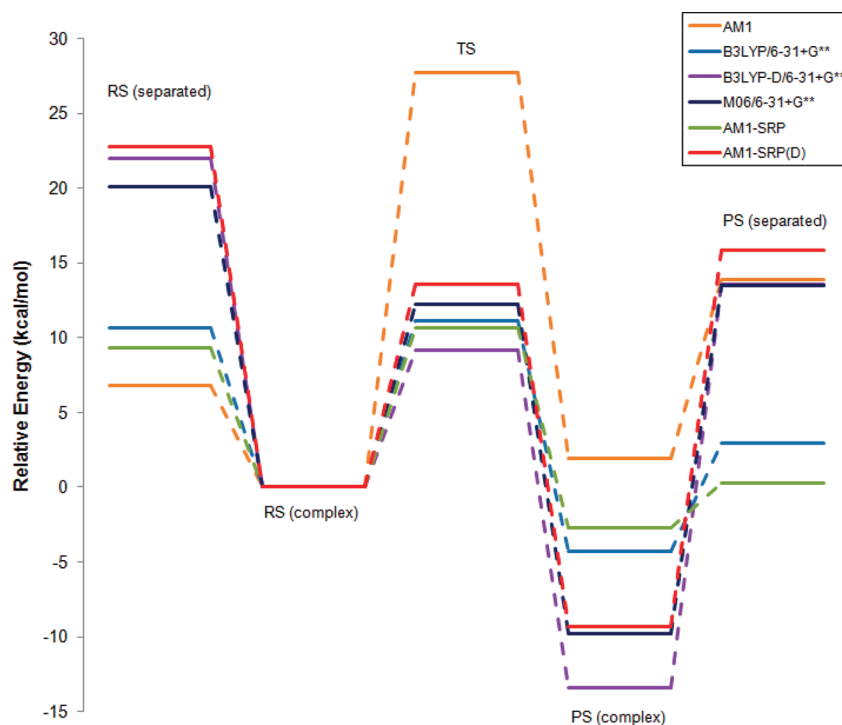


Figure 7. The relative energies of the reactant, transition and product states associated with the reaction $6\text{-Me-H}_3\text{pterin}^+ + \text{trans-Me-H}_2\text{nic} \rightarrow 6\text{-Me-H}_4\text{pterin} + \text{trans-Me-Hnic}^+$, for standard AM1, B3LYP/6-31+G**, B3LYP-D/6-31+G**, M06/6-31+G**, AM1-SRP, and AM1-SRP(D). The sums of the energies of the individual subunits for the reactants and products are represented by RS (separated) and PS (separated), respectively, where RS (complex) and PS (complex) refer to the corresponding bimolecular complexes.

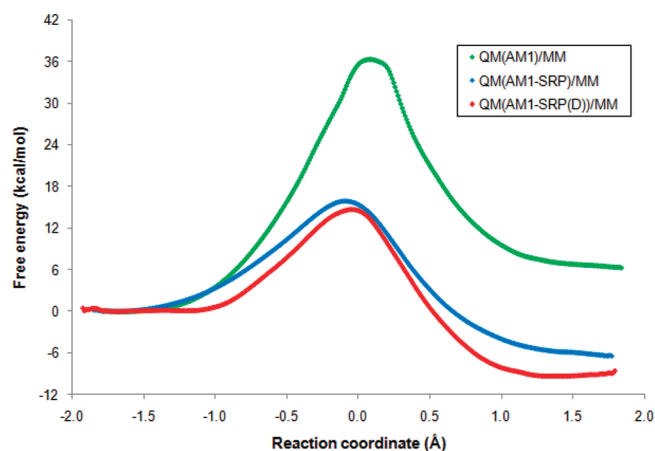


Figure 8. Computed classical potentials of mean force for the hydride transfer reaction catalyzed by *E. coli* DHFR at 298 K, obtained with three different QM/MM schemes distinguished by the semiempirical treatment of the QM region: AM1/MM (green), AM1-SRP/MM (blue), and AM1-SRP(D)/MM (red). The reaction coordinate is defined as the difference between the distances of the transferring hydride and the donor and acceptor carbon atoms.

6-31+G(d,p) basis set. BSSE corrections were included for the DFT methods but not for HF. The different semiempirical QM/MM methods give similar interaction energies, indicating that the SRP optimization process did not introduce artificial polarization of the molecules (Table S8b and Figure S2, Supporting Information). The QM/MM methods predict slightly weaker complexes than M06 and B3LYP-D (RMSDs of 2.6–4.4 kcal/mol),

while they are in good agreement with B3LYP and HF (RMSDs between 1.2 and 2.4 kcal/mol).

Enzyme Simulations. *Classical Potential of Mean Force.* Figure 8 shows the classical mechanical PMF (CM-PMF) for the hydride transfer reaction in DHFR obtained from free energy MD simulations, using the AM1, AM1-SRP, and AM1-SRP(D) QM/MM Hamiltonians. We note that these data are not directly comparable to experimental results as NQEs are not yet included at this stage. The AM1/MM Hamiltonian substantially overestimates the free energy barrier ($\Delta G^\ddagger = 36.3$ kcal/mol) and predicts an endothermic reaction ($\Delta G^r = 6.3$ kcal/mol). The transition state (the free energy bottleneck of the PMF) for the QM(AM1-SRP)/MM Hamiltonian is located at $\zeta^\ddagger = -0.089$ Å, whereas that of the QM(AM1-SRP(D))/MM Hamiltonian is placed at $\zeta^\ddagger = -0.045$ Å. Both are relatively late compared to that reported by Gao and co-workers in recent QM/MM studies ($\zeta^\ddagger = -0.145$ Å) on *ec*DHFR, which utilized the AM1 Hamiltonian with SVB correction (*vide supra*).^{7,8} We further note that the end points of the AM1-SRP and AM1-SRP(D) QM/MM free energy profiles are smooth and show no artificial free-energy increase. The classical free energies of reaction and activation extracted from the QM(AM1-SRP)/MM-based free energy profile are -6.4 and 15.9 kcal/mol. The CM-PMF obtained by the enhanced Hamiltonian, QM(AM1-SRP(D))/MM, predicts a classical mechanical free energy barrier which is narrower and slightly lower ($\Delta G^\ddagger = 14.7$ kcal/mol), and the reaction is more exergonic ($\Delta G^r = -9.3$ kcal/mol) by 3 kcal/mol. The considerable stabilization of the product state by ca. 5 kcal/mol compared with the experimental data is possibly a manifestation of the “over-stacking” phenomenon already encountered with the AM1-SRP(D) in the gas phase (*vide supra*). Finally, the differences

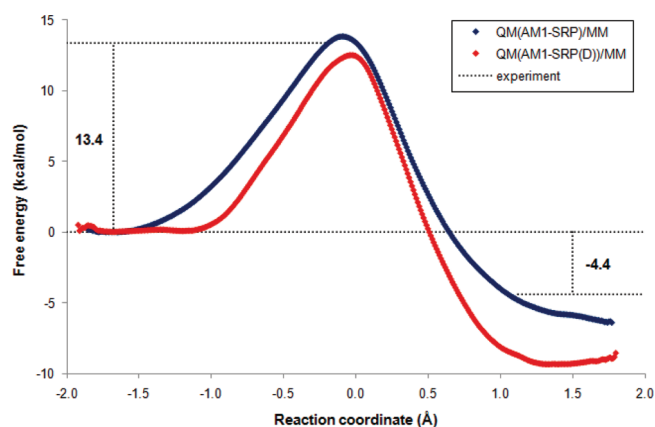


Figure 9. The quantum mechanical potentials of mean force for the hydride transfer reaction in *E. coli* DHFR. The centroid coordinates are used in path-integral simulations. Each quantized particle was represented by 32 beads. The experimental free energies of reaction and activation are denoted near the dashed lines.

in the free energy barrier width among the three QM/MM Hamiltonians are consistent with the trends in the imaginary vibrational frequency of the transition state in the gas phase obtained from the corresponding semiempirical schemes. According to Table 4, the imaginary wavenumbers in absolute values are ordered as follows: AM1 > AM1-SRP(D) > AM1-SRP. Indeed, the QM(AM1)/MM free energy profile has the narrowest barrier, that of QM(AM1-SRP(D))/MM is wider, and the QM(AM1-SRP)/MM Hamiltonian yields a PMF with the widest barrier.

Quantum Potential of Mean Force. The QM-PMF is obtained from Feynman path-integral calculations,^{46,86,88} in which the centroid positions of the discrete paths of quantized particles are used to specify the reaction coordinate.^{46,89,90} The “quantum” free energy profiles displayed in Figure 9 describe the hydride transfer reaction with the two SRP QM/MM Hamiltonians. Using QM(AM1-SRP)/MM, the inclusion of NQE in the simulations⁴⁶ lowers the computed free energies of activation for the hydride and deuteride transfer by 2.1 and 1.4 kcal/mol, respectively, relative to the “classical” free energy barrier. The resulting quantum free energies of reaction and activation for the hydride transfer, −6.4 and 13.8 kcal/mol, are in good accord with the corresponding experimental results (−4.4 and 13.4 kcal/mol).⁵ The quantum corrections for the AM1-SRP(D)/MM CM-PMF are very similar, 2.2 and 1.5 kcal/mol for hydride and deuteride, so that the predicted free energy barrier (12.5 kcal/mol) is in close agreement with experimental results. The free-energy results demonstrate that the present QM/MM and path integral methods can provide an adequate description of the hydride transfer reaction in DHFR.

Kinetic Isotope Effects. The computed primary ($k_{\text{H}}^{\text{H}}/k_{\text{D}}^{\text{H}}$) and secondary ($k_{\text{H}}^{\text{H}}/k_{\text{H}}^{\text{D}}$) KIEs for the hydride transfer reaction in DHFR at 298 K are 3.51 ± 0.14 and 1.18 ± 0.06 with QM(AM1-SRP)/MM and 3.49 ± 0.16 and 1.11 ± 0.04 with QM(AM1-SRP(D))/MM, respectively. These values are in good agreement with the experimental intrinsic KIEs measured by Kohen and co-workers ($k_{\text{H}}^{\text{H}}/k_{\text{D}}^{\text{H}} = 3.55 \pm 0.17$; $k_{\text{H}}^{\text{H}}/k_{\text{H}}^{\text{D}} = 1.13 \pm 0.01$),⁷² providing additional evidence for the accuracy of our computational treatments. These KIEs are also in good agreement with various QM/MM calculations (e.g., refs 7 (2° KIEs = 1.13) and 39 (1° KIEs = 3.4 ± 0.6)), but here the same method is within experimental error for both 1° and 2° KIEs.

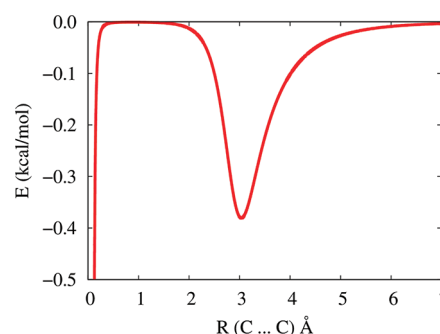


Figure 10. The dispersion energy between two carbon atoms calculated using Grimme's formula.

SUMMARY

In the current work, we presented extensive benchmark calculations for several model reactions in the gas phase that are relevant to the DHFR catalyzed hydride transfer. We employed G4MP2 and CBS-QB3 ab initio calculations as well as numerous density functional methods. Using these results as target data, we developed two specific reaction parameter (SRP) Hamiltonians by reparametrization of the semiempirical AM1 method. The first generation SRP Hamiltonian does not account for dispersion, while the second generation SRP includes dispersion implicitly via the AM1 core-repulsion functions. These SRP semiempirical Hamiltonians were subsequently used in hybrid quantum mechanics/molecular mechanics simulations of the DHFR catalyzed reaction. The classical PMFs were computed using the standard AM1 method as well as the AM1-SRP and AM1-SRP(D) models. Nuclear quantum effects were included using a Feynman path-integral method. Finally, kinetic isotope effects were computed using a mass-perturbation-based path-integral approach. The quantum PMFs predict free energy barriers and reaction free energies in good agreement with available experimental kinetic data.

We conclude that the resulting PESs yield accuracies comparable to those obtained at the G4MP2 and DFT levels, with a computational cost that is several orders of magnitude less. This will allow us to perform long MD simulations of the solvated enzyme, while providing a realistic description of the kinetics and thermodynamic properties in the DHFR catalyzed reaction.

APPENDIX A

The dispersion energies were estimated using the formula introduced by Grimme for density functional methods.

$$E_{\text{disp}}(r_{ij}) = -s_6 \sum_{i=1}^N \sum_{j=i+1}^{N-1} \frac{C_{6,ij}}{r_{ij}^6} f_d(r_{ij})$$

$$f_d(r_{ij}) = \frac{1}{1 + \exp\{-d[(r_{ij}/r_0) - 1]\}}$$

where r_{ij} is the distance between atoms i and j . s_6 is a global scaling factor for the dispersion energy, with numerical values ranging from 0.75 to 1.2 for different density functionals. Herein, we chose the value 1.0 for simplicity. d is a parameter for damping function f_d . It was chosen to be 20.0 in line with the value used in DFT-D2. The atomic C_6 coefficients and van der Waals radii r_0 were taken directly from the original publication. Figure 10 plots the calculated dispersion energy for two carbon atoms.

The sum of the standard AM1 core repulsion function and the dispersion energy correction was scanned for each atom pair. A total of 396 points for the carbon, nitrogen, and oxygen pairs and 346 points for the hydrogen pair were collected from a distance of 0.1 Å with a step size of 0.02 Å. Finally, the parameters in the Gaussian terms were fitted to these data points using a nonlinear least-squares procedure implemented in gnuplot with the standard AM1 parameters as an initial guess. The convergence criterion was 1.0×10^{-6} .

■ ASSOCIATED CONTENT

S Supporting Information. Comprehensive list of the gas phase molecular models; summary of recent computational studies on the DHFR-catalyzed hydride transfer reaction; vibrational frequency scale factors used for gas phase thermochemistry calculations; details of the development of AM1-SRP, calibration, and related target values; selected gas phase vibrational frequencies; list of the semiempirical parameters of AM1-SRP and AM1-SRP(D); coordinates of geometries calculated at the target levels; comparison between the crystal structure and computed geometry of 6-Me-H₃pterin⁺; ligand–water QM/MM complexation energies; and further details with regard to the MD simulations of the solvated enzyme. This material is available free of charge via the Internet at <http://pubs.acs.org>.

■ AUTHOR INFORMATION

Corresponding Author

*E-mail: majort@biu.ac.il.

■ ACKNOWLEDGMENT

This work has been supported by the Israel Science Foundation and the United States–Israel Binational Science Foundation (Grant # 2007256).

■ REFERENCES

- (1) Schnell, J. R.; Dyson, H. J.; Wright, P. E. Structure, dynamics, and catalytic function of dihydrofolate reductase. *Annu. Rev. Biophys. Biomol. Struct.* **2004**, *33*, 119–140.
- (2) Huennekens, F. In search of dihydrofolate reductase. *Protein Sci.* **1996**, *5*, 1201.
- (3) Frey, P. A.; Hegeman, A. D. *Enzymatic reaction mechanisms*; Oxford University Press: New York, 2007.
- (4) Castillo, R.; Andrés, J.; Moliner, V. Catalytic Mechanism of Dihydrofolate Reductase Enzyme. A Combined Quantum-Mechanical/Molecular-Mechanical Characterization of Transition State Structure for the Hydride Transfer Step. *J. Am. Chem. Soc.* **1999**, *121*, 12140–12147.
- (5) Fierke, C. A.; Johnson, K. A.; Benkovic, S. J. Construction and evaluation of the kinetic scheme associated with dihydrofolate reductase from *Escherichia coli*. *Biochemistry* **1987**, *26*, 4085–4092.
- (6) Morrison, J. F.; Stone, S. R. Mechanism of the reaction catalyzed by dihydrofolate reductase from *Escherichia coli*: pH and deuterium isotope effects with NADPH as the variable substrate. *Biochemistry* **1988**, *27*, 5499–5506.
- (7) Garcia-Viloca, M.; Truhlar, D. G.; Gao, J. Reaction-Path Energetics and Kinetics of the Hydride Transfer Reaction Catalyzed by Dihydrofolate Reductase. *Biochemistry* **2003**, *42*, 13558–13575.
- (8) Pu, J.; Ma, S.; Garcia-Viloca, M.; Gao, J.; Truhlar, D. G.; Kohen, A. Nonperfect Synchronization of Reaction Center Rehybridization in the Transition State of the Hydride Transfer Catalyzed by Dihydrofolate Reductase. *J. Am. Chem. Soc.* **2005**, *127*, 14879–14886.
- (9) Maharaj, G.; Selinsky, B.; Appleman, J.; Perlman, M.; London, R.; Blakley, R. Dissociation constants for dihydrofolic acid and dihydrobiopterin and implications for mechanistic models for dihydrofolate reductase. *Biochemistry* **1990**, *29*, 4554.
- (10) Chen, Y. Q.; Kraut, J.; Blakley, R. L.; Callender, R. Determination by Raman Spectroscopy of the pK_a of N5 of Dihydrofolate Bound to Dihydrofolate Reductase: Mechanistic Implications. *Biochemistry* **1994**, *33*, 7021–7026.
- (11) Deng, H.; Callender, R. Structure of Dihydrofolate When Bound to Dihydrofolate Reductase. *J. Am. Chem. Soc.* **1998**, *120*, 7730–7737.
- (12) Deng, H.; Callender, R.; Howell, E. Vibrational Structure of Dihydrofolate Bound to R67 Dihydrofolate Reductase. *J. Biol. Chem.* **2001**, *276*, 48956–48960.
- (13) Howell, E.; Villafranca, J.; Warren, M.; Oatley, S.; Kraut, J. Functional role of aspartic acid-27 in dihydrofolate reductase revealed by mutagenesis. *Science* **1986**, *231*, 1123–1128.
- (14) David, C. L.; Howell, E. E.; Farnum, M. F.; Villafranca, J. E.; Oatley, S. J.; Kraut, J. Structure and function of alternative proton-relay mutants of dihydrofolate reductase. *Biochemistry* **1992**, *31*, 9813–9822.
- (15) Chen, Y.; Kraut, J.; Callender, R. pH-dependent conformational changes in *Escherichia coli* dihydrofolate reductase revealed by Raman difference spectroscopy. *Biophys. J.* **1997**, *72*, 936–941.
- (16) Rod, T. H.; Brooks, C. L., III. How Dihydrofolate Reductase Facilitates Protonation of Dihydrofolate. *J. Am. Chem. Soc.* **2003**, *125*, 8718–8719.
- (17) Bolin, J.; Filman, D.; Matthews, D.; Hamlin, R.; Kraut, J. Crystal structures of *Escherichia coli* and *Lactobacillus casei* dihydrofolate reductase refined at 1.7 Å resolution. I. General features and binding of methotrexate. *J. Biol. Chem.* **1982**, *257*, 13650.
- (18) Bystroff, C.; Oatley, S.; Kraut, J. Crystal structures of *Escherichia coli* dihydrofolate reductase: The NADP⁺ holoenzyme and the folate·NADP⁺ ternary complex. Substrate binding and a model for the transition state. *Biochemistry* **1990**, *29*, 3263–3277.
- (19) Bystroff, C.; Kraut, J. Crystal structure of unliganded *Escherichia coli* dihydrofolate reductase. Ligand-induced conformational changes and cooperativity in binding. *Biochemistry* **1991**, *30*, 2227–2239.
- (20) Sawaya, M.; Kraut, J. Loop and Subdomain Movements in the Mechanism of *Escherichia coli* Dihydrofolate Reductase: Crystallographic Evidence. *Biochemistry* **1997**, *36*, 586–603.
- (21) Donkersloot, M. C. A.; Buck, H. M. The hydride-donation reaction of reduced nicotinamide adenine dinucleotide. 2. MINDO/3 and STO-3G calculations on the role of the carbamoyl group in enzymic reactions. *J. Am. Chem. Soc.* **1981**, *103*, 6554–6558.
- (22) Cummins, P. L.; Gready, J. E. Mechanistic aspects of biological redox reactions involving NADH 2: A combined semiempirical and *ab initio* study of hydride-ion transfer between the NADH analogue, 1-methyl-dihydronicotinamide, and folate and dihydrofolate analogue substrates of dihydrofolate reductase. *J. Comput. Chem.* **1990**, *11*, 791–804.
- (23) Andrés, J.; Safont, V. S.; Martins, J. B. L.; Beltrán, A.; Moliner, V. AM1 and PM3 transition structure for the hydride transfer. A model of reaction catalyzed by dihydrofolate reductase. *THEOCHEM* **1995**, *330*, 411–416.
- (24) Andrés, J.; Moliner, V.; Safont, V. S.; Domingo, L. R.; Picher, M. T.; Krechl, J. On Transition Structures for Hydride Transfer Step: A Theoretical Study of the Reaction Catalyzed by Dihydrofolate Reductase Enzyme. *Bioorg. Chem.* **1996**, *24*, 10–18.
- (25) Cummins, P. L.; Ramnarayan, K.; Singh, U. C.; Gready, J. E. Molecular dynamics/free energy perturbation study on the relative affinities of the binding of reduced and oxidized NADP to dihydrofolate reductase. *J. Am. Chem. Soc.* **1991**, *113*, 8247–8256.
- (26) Cummins, P. L.; Gready, J. E. Molecular dynamics and free energy perturbation study of hydride-ion transfer step in dihydrofolate reductase using combined quantum and molecular mechanical model. *J. Comput. Chem.* **1998**, *19*, 977–988.
- (27) Ferrer, S.; Silla, E.; Tuñón, I.; Martí, S.; Moliner, V. Catalytic Mechanism of Dihydrofolate Reductase Enzyme. A Combined Quantum-Mechanical/Molecular-Mechanical Characterization of the N5 Protonation Step. *J. Phys. Chem. B* **2003**, *107*, 14036–14041.

- (28) Cummins, P. L.; Greatbanks, S. P.; Rendell, A. P.; Gready, J. E. Computational Methods for the Study of Enzymic Reaction Mechanisms. 1. Application to the Hydride Transfer Step in the Catalysis of Dihydrofolate Reductase. *J. Phys. Chem. B* **2002**, *106*, 9934–9944.
- (29) Thorpe, I. F.; Brooks, C. L. Barriers to Hydride Transfer in Wild Type and Mutant Dihydrofolate Reductase from *E. coli*. *J. Phys. Chem. B* **2003**, *107*, 14042–14051.
- (30) Thorpe, I. F.; Brooks, C. L. Conformational Substates Modulate Hydride Transfer in Dihydrofolate Reductase. *J. Am. Chem. Soc.* **2005**, *127*, 12997–13006.
- (31) Ranganathan, S.; Gready, J. E. Hybrid Quantum and Molecular Mechanical (QM/MM) Studies on the Pyruvate to L-Lactate Interconversion in L-Lactate Dehydrogenase. *J. Phys. Chem. B* **1997**, *101*, 5614–5618.
- (32) Turner, A.; Moliner, V.; Williams, I. Transition-state structural refinement with GRACE and CHARMM: Flexible QM/MM modelling for lactate dehydrogenase. *Phys. Chem. Chem. Phys.* **1999**, *1*, 1323–1331.
- (33) Faulder, P. F.; Tresadern, G.; Chohan, K. K.; Scrutton, N. S.; Sutcliffe, M. J.; Hillier, I. H.; Burton, N. A. QM/MM Studies Show Substantial Tunneling for the Hydrogen-Transfer Reaction in Methylamine Dehydrogenase. *J. Am. Chem. Soc.* **2001**, *123*, 8604–8605.
- (34) Ferrer, S.; Ruiz-Pernía, J. J.; Tuñón, I.; Moliner, V.; Garcia-Viloca, M.; González-Lafont, A.; Lluch, J. M. A QM/MM Exploration of the Potential Energy Surface of Pyruvate to Lactate Transformation Catalyzed by LDH. Improving the Accuracy of Semiempirical Descriptions. *J. Chem. Theory Comput.* **2005**, *1*, 750–761.
- (35) Devi-Kesavan, L. S.; Garcia-Viloca, M.; Gao, J. Semiempirical QM/MM potential with simple valence bond (SVB) for enzyme reactions. Application to the nucleophilic addition reaction in haloalkane dehalogenase. *Theor. Chem. Acc.* **2003**, *109*, 133–139.
- (36) Truhlar, D. G.; Gao, J.; Alhambra, C.; Garcia-Viloca, M.; Corchado, J.; Sánchez, M. L.; Villà, J. The Incorporation of Quantum Effects in Enzyme Kinetics Modeling. *Acc. Chem. Res.* **2002**, *35*, 341–349.
- (37) Warshel, A.; Weiss, R. M. An empirical valence bond approach for comparing reactions in solutions and in enzymes. *J. Am. Chem. Soc.* **1980**, *102*, 6218–6226.
- (38) Warshel, A. *Computer Modeling of Chemical Reactions in Enzymes*; Wiley: New York, 1991.
- (39) Agarwal, P. K.; Billeter, S. R.; Hammes-Schiffer, S. Nuclear quantum effects and enzyme dynamics in dihydrofolate reductase catalysis. *J. Phys. Chem. B* **2002**, *106*, 3283–3293.
- (40) Wong, K. F.; Selzer, T.; Benkovic, S. J.; Hammes-Schiffer, S. Chemical theory and computation special feature: impact of distal mutations on the network of coupled motions correlated to hydride transfer in dihydrofolate reductase. *Proc. Nat. Acad. Sci. U.S.A.* **2005**, *102*, 6807–6812.
- (41) Liu, H.; Warshel, A. The Catalytic Effect of Dihydrofolate Reductase and Its Mutants Is Determined by Reorganization Energies. *Biochemistry* **2007**, *46*, 6011–6025.
- (42) Hwang, J. K.; Warshel, A. A quantized classical path approach for calculations of quantum mechanical rate constants. *J. Phys. Chem.* **1993**, *97*, 10053–10058.
- (43) Rossi, I.; Truhlar, D. G. Parameterization of NDDO wavefunctions using genetic algorithms. An evolutionary approach to parameterizing potential energy surfaces and direct dynamics calculations for organic reactions. *Chem. Phys. Lett.* **1995**, *233*, 231–236.
- (44) Major, D. T.; York, D. M.; Gao, J. L. Solvent polarization and kinetic isotope effects in nitroethane deprotonation and implications to the nitroalkane oxidase reaction. *J. Am. Chem. Soc.* **2005**, *127*, 16374–16375.
- (45) Gao, J. L.; Wong, K. Y.; Major, D. T. Combined QM/MM and path integral simulations of kinetic isotope effects in the proton transfer reaction between nitroethane and acetate ion in water. *J. Comput. Chem.* **2008**, *29*, 514–522.
- (46) Major, D. T.; Gao, J. L. An integrated path integral and free-energy perturbation-umbrella sampling method for computing kinetic isotope effects of chemical reactions in solution and in enzymes. *J. Chem. Theory Comput.* **2007**, *3*, 949–960.
- (47) Major, D. T.; Gao, J. L. A combined quantum mechanical and molecular mechanical study of the reaction mechanism and alpha-amino acidity in alanine racemase. *J. Am. Chem. Soc.* **2006**, *128*, 16345–16357.
- (48) Major, D. T.; Heroux, A.; Orville, A. M.; Valley, M. P.; Fitzpatrick, P. F.; Gao, J. Differential quantum tunneling contributions in nitroalkane oxidase catalyzed and the uncatalyzed proton transfer reaction. *Proc. Natl. Acad. Sci. U.S.A.* **2009**, *106*, 20734–20739.
- (49) Frisch, M. J.; Trucks, G. W.; Schlegel, H. B.; Scuseria, G. E.; Robb, M. A.; Cheeseman, J. R.; Scalmani, G.; Barone, V.; Mennucci, B.; Petersson, G. A.; Nakatsuji, H.; Caricato, M.; Li, X.; Hratchian, H. P.; Izmaylov, A. F.; Bloino, J.; Zheng, G.; Sonnenberg, J. L.; Hada, M.; Ehara, M.; Toyota, K.; Fukuda, R.; Hasegawa, J.; Ishida, M.; Nakajima, T.; Honda, Y.; Kitao, O.; Nakai, H.; Vreven, T.; Montgomery, J. A., Jr.; Peralta, J. E.; Ogliaro, F.; Bearpark, M.; Heyd, J. J.; Brothers, E.; Kudin, K. N.; Staroverov, V. N.; Kobayashi, R.; Normand, J.; Raghavachari, K.; Rendell, A.; Burant, J. C.; Iyengar, S. S.; Tomasi, J.; Cossi, M.; Rega, N.; Millam, N. J.; Klene, M.; Knox, J. E.; Cross, J. B.; Bakken, V.; Adamo, C.; Jaramillo, J.; Gomperts, R.; Stratmann, R. E.; Yazyev, O.; Austin, A. J.; Cammi, R.; Pomelli, C.; Ochterski, J. W.; Martin, R. L.; Morokuma, K.; Zakrzewski, V. G.; Voth, G. A.; Salvador, P.; Dannenberg, J. J.; Dapprich, S.; Daniels, A. D.; Farkas, Ö.; Foresman, J. B.; Ortiz, J. V.; Cioslowski, J.; Fox, D. J. *Gaussian 09*, revision B.01; Gaussian, Inc.: Wallingford, CT, 2009.
- (50) Perdew, J. P.; Burke, K.; Ernzerhof, M. Generalized Gradient Approximation Made Simple. *Phys. Rev. Lett.* **1996**, *77*, 3865.
- (51) Adamo, C.; Cossi, M.; Barone, V. An accurate density functional method for the study of magnetic properties: the PBE0 model. *THEOCHEM* **1999**, *493*, 145–157.
- (52) Becke, A. D. Density-functional thermochemistry. III. The role of exact exchange. *J. Chem. Phys.* **1993**, *98*, 5648–5652.
- (53) Lee, C.; Yang, W.; Parr, R. G. Development of the Colle-Salvetti correlation-energy formula into a functional of the electron density. *Phys. Rev. B: Condens. Matter* **1988**, *37*, 785.
- (54) Stephens, P. J.; Devlin, F. J.; Chabalowski, C. F.; Frisch, M. J. *Ab Initio* Calculation of Vibrational Absorption and Circular Dichroism Spectra Using Density Functional Force Fields. *J. Phys. Chem.* **1994**, *98*, 11623–11627.
- (55) Schmider, H. L.; Becke, A. D. Optimized density functionals from the extended G2 test set. *J. Chem. Phys.* **1998**, *108*, 9624–9631.
- (56) Zhao, Y.; Lynch, B. J.; Truhlar, D. G. Development and Assessment of a New Hybrid Density Functional Model for Thermochemical Kinetics. *J. Phys. Chem. A* **2004**, *108*, 2715–2719.
- (57) Zhao, Y.; Truhlar, D. The M06 suite of density functionals for main group thermochemistry, thermochemical kinetics, noncovalent interactions, excited states, and transition elements: two new functionals and systematic testing of four M06-class functionals and 12 other functionals. *Theor. Chem. Acc.* **2008**, *120*, 215–241.
- (58) Dewar, M. J. S.; Zoebisch, E. G.; Healy, E. F.; Stewart, J. J. P. AM1: a new general purpose quantum mechanical molecular model. *J. Am. Chem. Soc.* **1985**, *107*, 3902–3909.
- (59) Montgomery, J. J. A.; Frisch, M. J.; Ochterski, J. W.; Petersson, G. A. A complete basis set model chemistry. VII. Use of the minimum population localization method. *J. Chem. Phys.* **2000**, *112*, 6532–6542.
- (60) Montgomery, J. J. A.; Frisch, M. J.; Ochterski, J. W.; Petersson, G. A. A complete basis set model chemistry. VI. Use of density functional geometries and frequencies. *J. Chem. Phys.* **1999**, *110*, 2822–2827.
- (61) Curtiss, L. A.; Redfern, P. C.; Raghavachari, K. Gaussian-4 theory. *J. Chem. Phys.* **2007**, *126*, 084108–12.
- (62) Curtiss, L. A.; Redfern, P. C.; Raghavachari, K. Gaussian-4 theory using reduced order perturbation theory. *J. Chem. Phys.* **2007**, *127*, 124105.
- (63) Armarego, W. L. F.; Waring, P.; Williams, J. W. Absolute configuration of 6-methyl-5,6,7,8-tetrahydropterin produced by enzymic reduction (dihydrofolate reductase and NADPH) of 6-methyl-7,8-dihydropterin. *J. Chem. Soc., Chem. Commun.* **1980**, 334–336.
- (64) Peng, C.; Schlegel, H. B. Combining synchronous transit and quasi-Newton methods to find transition states. *Isr. J. Chem.* **1994**, *33*, 449–54.

- (65) Grimme, S. Semiempirical GGA-type density functional constructed with a long-range dispersion correction. *J. Comput. Chem.* **2006**, *27*, 1787–1799.
- (66) Schwabe, T.; Grimme, S. Double-hybrid density functionals with long-range dispersion corrections: higher accuracy and extended applicability. *Phys. Chem. Chem. Phys.* **2007**, *9*, 3397–3406.
- (67) Benach, J.; Atrian, S.; González-Duarte, R.; Ladenstein, R. The catalytic reaction and inhibition mechanism of *Drosophila* alcohol dehydrogenase: observation of an enzyme-bound NAD-ketone adduct at 1.4 Å resolution by X-ray crystallography. *J. Mol. Biol.* **1999**, *289*, 335–355.
- (68) Kavanagh, K. L.; Klimacek, M.; Nidetzky, B.; Wilson, D. K. Crystal Structure of *Pseudomonas fluorescens* Mannitol 2-Dehydrogenase Binary and Ternary Complexes. *J. Biol. Chem.* **2002**, *277*, 43433–43442.
- (69) Major, D. T.; Nam, K.; Gao, J. L. Transition state stabilization and alpha-amino carbon acidity in alanine racemase. *J. Am. Chem. Soc.* **2006**, *128*, 8114–8115.
- (70) Gready, J. E. Theoretical studies on the activation of the pterin cofactor in the catalytic mechanism of dihydrofolate reductase. *Biochemistry* **1985**, *24*, 4761–4766.
- (71) Rajagopalan, P.; Lutz, S.; Benkovic, S. Coupling interactions of distal residues enhance dihydrofolate reductase catalysis: mutational effects on hydride transfer rates. *Biochemistry* **2002**, *41*, 12618–12628.
- (72) Sikorski, R. S.; Wang, L.; Markham, K. A.; Rajagopalan, P. T. R.; Benkovic, S. J.; Kohen, A. Tunneling and coupled motion in the *E. coli* dihydrofolate reductase catalysis. *J. Am. Chem. Soc.* **2004**, *126*, 4778–4779.
- (73) Brooks, B. R.; Brucoleri, R. E.; Olafson, B. D.; States, D. J.; Swaminathan, S.; Karplus, M. CHARMM: A program for macromolecular energy, minimization, and dynamics calculations. *J. Comput. Chem.* **1983**, *4*, 187–217.
- (74) Brooks, B. R., III; C. L., B., Jr.; Nilsson, L.; Petrella, R. J.; Roux, B.; Won, Y.; Archontis, G.; Bartels, C.; Boresch, S.; Caffisch, A.; Caves, L.; Cui, Q.; Dinner, A. R.; Feig, M.; Fischer, S.; Gao, J.; Hodoseck, M.; Im, W.; Kuczera, K.; Lazaridis, T.; Ma, J.; Ovchinnikov, V.; Paci, E.; Pastor, R. W.; Post, C. B.; Pu, J. Z.; Schaefer, M.; Tidor, B.; Venable, R. M.; Woodcock, H. L.; Wu, X.; Yang, W.; York, D. M.; Karplus, M. CHARMM: The biomolecular simulation program. *J. Comput. Chem.* **2009**, *30*, 1545–1614.
- (75) Sem, D. S.; Kasper, C. B. Enzyme-substrate binding interactions of NADPH-cytochrome P-450 oxidoreductase characterized with pH and alternate substrate/inhibitor studies. *Biochemistry* **1993**, *32*, 11539–11547.
- (76) Khavrutskii, I.; Price, D.; Lee, J.; Brooks, C., III. Conformational change of the methionine 20 loop of *Escherichia coli* dihydrofolate reductase modulates pKa of the bound dihydrofolate. *Protein Sci.* **2007**, *16*, 1087.
- (77) Stone, D.; Paterson, S. J.; Raper, J. H.; Phillips, A. W. The amino acid sequence of dihydrofolate reductase from the mouse lymphoma L1210. *J. Biol. Chem.* **1979**, *254*, 480–488.
- (78) Smith, D. R.; Calvo, J. M. Nucleotide sequence of the *E. coli* gene coding for dihydrofolate reductase. *Nucleic Acids Res.* **1980**, *8*, 2255–2274.
- (79) Murzina, N. V.; Gudkov, A. T. Invariant amino acid replacement affects the dihydrofolate reductase function and its gene expression. *Protein Eng.* **1990**, *3*, 709–712.
- (80) Allen, M. P.; Tildesley, D. J. *Computer Simulation of Liquids*; Oxford University Press: Oxford, U. K., 1987; pp 156–162.
- (81) MacKerell, A. D.; Bashford, D.; Bellott, Dunbrack, R. L.; Evanseck, J. D.; Field, M. J.; Fischer, S.; Gao, J.; Guo, H.; Ha, S.; Joseph-McCarthy, D.; Kuchnir, L.; Kuczera, K.; Lau, F. T. K.; Mattos, C.; Michnick, S.; Ngo, T.; Nguyen, D. T.; Prodhom, B.; Reiher, W. E.; Roux, B.; Schlenkrich, M.; Smith, J. C.; Stote, R.; Straub, J.; Watanabe, M.; Wiorkiewicz-Kuczera, J.; Yin, D.; Karplus, M. All-Atom Empirical Potential for Molecular Modeling and Dynamics Studies of Proteins. *J. Phys. Chem. B* **1998**, *102*, 3586–3616.
- (82) MacKerell, A. D.; Feig, M.; Brooks, C. L., III. Extending the treatment of backbone energetics in protein force fields: Limitations of gas-phase quantum mechanics in reproducing protein conformational distributions in molecular dynamics simulations. *J. Comput. Chem.* **2004**, *25*, 1400–1415.
- (83) Jorgensen, W. L.; Chandrasekhar, J.; Madura, J. D.; Impey, R. W.; Klein, M. L. Comparison of simple potential functions for simulating liquid water. *J. Chem. Phys.* **1983**, *79*, 926–935.
- (84) Gao, J. Toward a Molecular Orbital Derived Empirical Potential for Liquid Simulations. *J. Phys. Chem. B* **1997**, *101*, 657–663.
- (85) Sprik, M.; Klein, M. L.; Chandler, D. Staging - a sampling technique for the Monte-Carlo evaluation of path-integrals. *Phys. Rev. B: Condens. Matter* **1985**, *31*, 4234–4244.
- (86) Major, D. T.; Garcia-Viloca, M.; Gao, J. L. Path integral simulations of proton transfer reactions in aqueous solution using combined QM/MM potentials. *J. Chem. Theory Comput.* **2006**, *2*, 236–245.
- (87) Hwang, J. K.; Chu, Z. T.; Yadav, A.; Warshel, A. Simulations of quantum mechanical corrections for rate constants of hydride-transfer reactions in enzymes and solutions. *J. Phys. Chem.* **1991**, *95*, 8445–8448.
- (88) Major, D. T.; Gao, J. L. Implementation of the bisection sampling method in path integral simulations. *J. Mol. Graphics Modell.* **2005**, *24*, 121–127.
- (89) Cao, J.; Voth, G. A. A unified framework for quantum activated rate processes. I. General theory. *J. Chem. Phys.* **1996**, *105*, 6856–6870.
- (90) Gillan, M. J. Quantum simulation of hydrogen in metals. *Phys. Rev. Lett.* **1987**, *58*, 563.
- (91) Nam, K.; Gao, J.; York, D. M. An Efficient Linear-Scaling Ewald Method for Long-Range Electrostatic Interactions in Combined QM/MM Calculations. *J. Chem. Theory Comput.* **2005**, *1*, 2–13.
- (92) Andersen, H. C. Molecular dynamics simulations at constant pressure and/or temperature. *J. Chem. Phys.* **1980**, *72*, 2384–2393.
- (93) Hoover, W. G. Canonical dynamics: Equilibrium phase-space distributions. *Phys. Rev. A: At. Mol. Opt. Phys.* **1985**, *31*, 1695.
- (94) Ryckaert, J.-P.; Ciccotti, G.; Berendsen, H. J. C. Numerical integration of the cartesian equations of motion of a system with constraints: molecular dynamics of n-alkanes. *J. Comput. Phys.* **1977**, *23*, 327–341.
- (95) Pu, J.; Gao, J.; Truhlar, D. G. Multidimensional Tunneling, Recrossing, and the Transmission Coefficient for Enzymatic Reactions. *Chem. Rev.* **2006**, *106*, 3140–3169.
- (96) Torrie, G. M.; Valleau, J. P. Nonphysical sampling distributions in Monte Carlo free-energy estimation: Umbrella sampling. *J. Comput. Phys.* **1977**, *23*, 187–199.
- (97) Kumar, S.; Rosenberg, J. M.; Bouzida, D.; Swendsen, R. H.; Kollman, P. A. The weighted histogram analysis method for free-energy calculations on biomolecules. I. The method. *J. Comput. Chem.* **1992**, *13*, 1011–1021.
- (98) Bieri, J. The crystal structure of 6-methyl-7,8-dihydropterine-mono-hydrochloride-mono-hydrate. *Helv. Chim. Acta* **1977**, *60*, 2303–2308.
- (99) Weber, R.; Viscontini, M. Über Pterinchemie 53. Mitteilung: Zur Konformation von 6-Methyl- und 5,6-Dimethyl-5,6,7,8-tetrahydropterin in wässriger Lösung. *Helv. Chim. Acta* **1975**, *58*, 1772–1780.
- (100) Poe, M.; Hoogsteen, K. 5,6,7,8-Tetrahydrofolic acid. Conformation of the tetrahydropyrazine ring. *J. Biol. Chem.* **1978**, *253*, 543–546.
- (101) Ganguly, A. N.; Bieri, J. H.; Viscontini, M. Über Pterinchemie. 77. Mitteilung: Das (6R,S)-5-Formyl-6-methyl-5,6,7,8-tetrahydropterin: Synthese, chemische und physikalisch-chemische Eigenschaften. *Helv. Chim. Acta* **1981**, *64*, 367–372.
- (102) Williams, T. C.; Strom, C. B. Tetrahydrobiopterin analogs: the solution conformations of 6-methyltetrahydropterin, 7-methyltetrahydropterin, and cis- and trans-6,7-dimethyltetrahydropterins as determined by proton nuclear magnetic resonance. *Biochemistry* **1985**, *24*, 458–466.
- (103) Yamada, T.; Liu, X.; Englert, U.; Yamane, H.; Dronskowski, R. Solid-State Structure of Free Base Guanidine Achieved at Last. *Chem.—Eur. J.* **2009**, *15*, S651–S655.
- (104) Caminiti, R.; Pieretti, A.; Bencivenni, L.; Ramondo, F.; Sanna, N. Amidine N—C(N)—N Skeleton: Its Structure in Isolated and Hydrogen-Bonded Guanidines from ab Initio Calculations. *J. Phys. Chem.* **1996**, *100*, 10928–10935.
- (105) Zhong, H.; Bowen, J. P. Theoretical study of stereoselective reduction controlled by NADH analogs. *J. Mol. Graphics Modell.* **2005**, *24*, 1–9.

(106) Cummins, P. L.; Gready, J. E. Mechanistic aspects of biological redox reactions involving NADH 1: Ab initio quantum chemical structures of the 1-methyl-nicotinamide and 1-methyl-dihydronicotinamide coenzyme analogues. *THEOCHEM* **1989**, *183*, 161–174.

(107) Wu, Y. D.; Houk, K. N. Theoretical study of conformational features of NAD⁺ and NADH analogs: protonated nicotinamide and 1,4-dihydronicotinamide. *J. Org. Chem.* **1993**, *58*, 2043–2045.

(108) Almarsson, Ö.; Bruice, T. C. Evaluation of the factors influencing reactivity and stereospecificity in NAD(P)H dependent dehydrogenase enzymes. *J. Am. Chem. Soc.* **2002**, *115*, 2125–2138.

(109) Karle, I. The crystal structure of N-benzyl-1,4-dihydronicotinamide. *Acta Crystallogr.* **1961**, *14*, 497–502.

(110) Glasfeld, A.; Zbinden, P.; Dobler, M.; Benner, S. A.; Dunitz, J. D. Crystal structures of two simple N-substituted dihydronicotinamides: possible implications for stereoelectronic arguments in enzymology. *J. Am. Chem. Soc.* **1988**, *110*, 5152–5157.

■ NOTE ADDED AFTER ASAP PUBLICATION

This article was published ASAP on September 14, 2011. A change has been made to the caption of Figure 4. The correct version was published on September 21, 2011.